Ma Ying Juan (Orcid ID: 0000-0003-2584-7091)
Dong Chuanfei (Orcid ID: 0000-0002-8990-094X)
Toth Gabor (Orcid ID: 0000-0002-5654-9823)
Nagy Andrew F., F. (Orcid ID: 0000-0003-2617-9259)
Russell Christopher, T. (Orcid ID: 0000-0003-1639-8298)
Bougher Stephen, W. (Orcid ID: 0000-0002-4178-2729)
Fang Xiaohua (Orcid ID: 0000-0002-6584-2837)
Halekas Jasper, S. (Orcid ID: 0000-0001-5258-6128)
Espley Jared, Randolph (Orcid ID: 0000-0002-6371-9683)
Mahaffy Paul, R. (Orcid ID: 0000-0003-1896-1726)
Jakosky Bruce, M. (Orcid ID: 0000-0002-0758-9976)

Importance of ambipolar electric field in driving ion loss from Mars- Results from a multi-fluid MHD model with the electron pressure equation included

Y. J. Ma[1], C. F. Dong[2], G. Toth[3], B. van der Holst[3], A. F. Nagy[3], C. T. Russell[1], S. Bougher[3], Xiaohua Fang[4], J. S. Halekas[5], J. R. Espley[6], P. R. Mahaffy[6], M. Benna[6], J. McFadden[7], and B. M. Jakosky[4]

[1]Department of Earth Planetary and Space Sciences, UCLA, Los Angeles, CA, USA
[2]Department of Astrophysical Sciences and Princeton Plasma Physics Laboratory, Princeton University, Princeton, NJ, USA
[3]Department of Atmospheric, Oceanic and Space Sciences, University of Michigan, Ann Arbor, MI, USA
[4]Laboratory for Atmospheric and Space Physics, University of Colorado, Boulder, CO, USA
[5]Department of Physics and Astronomy, University of Iowa, Iowa City, IA, USA
[6]NASA Goddard Space Flight Center, Greenbelt, MD, USA
[7]Space Sciences Laboratory, University of California, Berkeley, California, USA

Key points:

1. For the first time, the effect of the ambipolar electric field is self-consistently included in the global multi-fluid MHD model.
2. The ambipolar electric field plays a significant role in driving ion loss from Mars. The ion mass loss can be enhanced by more than 50%.
3. The improved model matches best with MAVEN observations in comparsion with previous models.

Abstract

The multi-fluid (MF) magnetohydrodynamic (MHD) model of Mars is improved by solving an additional electron pressure equation. Through the electron pressure equation, the electron temperature is calculated based on the effects from various electron-related heating and cooling processes (e.g. photo-electron heating, electron-neutral collision and electron-ion collision), and thus the improved model can calculate the electron temperature and the electron pressure force

This is the author manuscript accepted for publication and has undergone full peer review but has not been through the copyediting, typesetting, pagination and proofreading process, which may lead to differences between this version and the Version of Record. Please cite this article as doi: 10.1029/2019JA027091

terms self-consistently. Model results of a typical case using the MFPe (multi-fluid with electron pressure equation included) model are compared in detail to identical cases using the MF and multi-species(MS) models to identify the effect of the improved physics. We find that when the electron pressure equation is included, the general interaction patterns are similar to those with no electron pressure equation. However, the MFPe model predicts that the electron temperature is much larger than the ion temperature in the ionosphere, consistent with both Viking and MAVEN observations. Using our numerical model, we also examined in detail the relative importance of different forces in the plasma interaction region. All three models are also applied to a MAVEN event study using identical input conditions; overall, the improved model matches best with MAVEN observations. All of the simulation cases are examined in terms of the total ion loss, and the results show that the inclusion of the electron pressure equation increases the escape rates by 50%-110% in total mass, depending on solar condition and strong crustal field orientation, clearly demonstrating the importance of the ambipolar electric field in facilitating ion escape.

1. Introduction

At Earth, there are two principal pathways to generate ionospheric outflows: Poynting flux and electron precipitation [*Strangeway et al.*, 2005]. Although both processes lead to an increase in ion scale height and ion upwelling, the former does so through Joule dissipation, while the latter does so through electron heating/ionization, which enhances the ambipolar electric field. The ambipolar electric field, also known as the electron pressure gradient force, plays an important role in driving ion acceleration along open magnetic field lines, and forming a polar wind in the polar cap region [*Axford*, 1968; *Banks and Holzer*, 1968; *Ganguli et al*., 1996; *Yau et al.*, 2007; *Welling et al.*, 2015].

In comparison, Mars does not have a substantial internal planetary magnetic field on a global scale, but has remanent crustal magnetic fields mostly located in the southern hemisphere [*Acuña et al.*, 1998, 1999]. Therefore, its interaction with the solar wind is mainly the ionosphere-atmosphere type of interaction, similar to that of Venus. However, the presence of the strong localized crustal magnetic fields significantly increases the complexity of the interaction，making its plasma environment and magnetic field topology unique in the solar system, akin to a mixture of Venus and Earth, with a globally induced magnetosphere [*Bertucci et al.*, 2011] but with mini-magnetospheres (local regions in which both sides of magnetic field lines are connected to the planet) around strong crustal field regions [*Mitchell et al.*, 2001; *Nagy et al.*, 2004].

The understanding of the solar wind-Mars interaction has been greatly improved by the observations of Mars Global Surveyor (MGS [*Brain et al.*, 2006], Mars Express (MEX) [*Barabash et al*., 2007] and the ongoing Mars Atmosphere and Volatile EvolutioN (MAVEN) mission [*Jakosky et al.*, 2015]. The measurements made by the MGS magnetometer/electron reflectometer(MAG/ER) have shown spatially localized enhancements in electron fluxes over the

strong crustal fields on both the dayside and night, indicating solar wind electron precipitation into the Martian upper atmosphere through the cusps of strong crustal fields [*Xu et al*., 2014]. Recent observations by the Langmuir Probe and Wave (LPW) instrument [*Andersson et al.*, 2015] on board MAVEN revealed that the electron temperature (Te) of the daytime ionosphere above 180 km altitude is higher than predicted [*Ergun et al.*, 2016], suggesting that the ambipolar electric field may play a more important role in driving ion loss from Mars.

Collinson et al. [2015] first provided an upper limit of ±2 V of the total potential drop in the Martian ionosphere by examining the photoelectron spectra measured by the MAVEN Solar Wind Electron Analyzer (SWEA) instrument [*Mitchell et al.*, 2016]. They later found that there was a large (7.7 ± 0.6 V) parallel potential drop above the Utopia Planitia, a large impact basin with no significant crustal magnetic field [*Collinson et al.*, 2016]. Recently, *Xu et al*. [2018] made a more accurate estimate of the magnitude of the ambipolar electric field on Mars, by combining measurements from the SupraThermal and Thermal Ion Compostion (STATIC) [*McFadden et al.*, 2015] and SWEA. According to the new method, the field alignment potential has an average value ranging from 0 to 1.5 V, smaller than the energy required for planetary ionospheric ions to overcome gravity (2.1 eV for O^+, and 4.2 eV for O_2^+).

There also has been some numerical work to quantify the effect of the ambipolar electric field. *Ergun et al*. [2016] evaluated the effect using a one-dimensional Combined Photochemistry and Ion Tracing (CAPIT) model, with prescribed electron temperature profile, and found that the ambipolar electric field from heated electrons can substantially increase ion outflow (O^+, O_2^+, and CO_2^+) in the present day. However, the effect has not been investigated on a global scale in a self-consistent manner. The ambipolar electric field is generally included in both global MHD or hybrid models, but the electron temperature is typically assumed to be constant [*Kallio et al.*, 2010; *Brecht and Ledvina*, 2010] or adiabatic [*Brecht and Ledvina*, 2014; *Brecht et al*., 2016; *Modolo et al*., 2016] in the hybrid model or the same as the ion temperature in the MHD model [*Ma et al.*, 2004; *Najib et al.*, 2011, *Dong C. et al.*, 2015]. The latter assumption is reasonable inside the deep ionosphere, where the neutral density is so dense that collisions between ions (and electrons) and neutrals are frequent; as a result, both the ion temperature and electron temperature are tightly coupled with the neutral temperature. However, it is often not the case in other plasma regions such as the upper ionosphere, induced magnetosphere, magnetosheath, and in solar wind. To accurately calculate the electron temperature and electron pressure force, a separate electron pressure equation is needed in the model. As shown in *Ma et al.* [2011], the inclusion of the electron pressure equation in the Titan MHD model leads to a significantly improved agreement between the model field and Cassini magnetometer data in the ionosphere.

In this study, the multi-fluid MHD (MF) model is further improved by including an electron pressure equation to self-consistently calculate the electron temperature and the electron pressure gradient force. In addition, some chemical reactions such as dissociative recombination reactions

(e.g. $O_2^+ + e \rightarrow O + O$ and $CO_2^+ + e \rightarrow CO + O$) and electron impact ionization rates are dependent on the electron temperature. Thus, improvement of the model is expected to lead to a more accurate description of both the plasma interaction with the solar wind and the ion density in the ionosphere. The rest of the paper is organized as follows: A detailed description of the MFPe model (i.e., improved multi-fluid MHD model with electron Pressure (Pe) equations included) is described in section 2. Model results are presented in section 3. We first present results from the MFPe model in section 3.1. Comparisons of MFPe model results with the MS (multi-species), and the MF (multi-fluid) models are provided in section 3.2. The effects of different forces and current distribution are discussed in section 3.3. A MAVEN case study is shown in section 3.4. Model results of ion escape rates are discussed in section 3.5. A brief summary and some discussion are presented in section 4.

2. Methodology: MFPe Model

The improved multi-fluid MHD model of Mars solves for the continuity, momentum, and pressure of the 4 ion fluids (H^+, O^+, O_2^+, CO_2^+), together with an electron pressure equation and magnetic induction equation. The continuity, momentum and magnetic induction equations are the same as in *Najib et al.* [2011], also listed below for completeness:

Continuity equations for each ion fluid:

$$\frac{\partial \rho_i}{\partial t} + \nabla \cdot (\rho_i \mathbf{u}) = S_i - L_i$$
$$S_i = m_i n_{i'} (\nu_{ph,i'} + \nu_{imp,i'} + \sum_{s=ions} k_{si'} n_s) \quad (1)$$
$$L_i = m_i n_i (\alpha_{R,i} n_e + \sum_{t=neutrals} k_{it} n_t)$$

where ρ_i (i=1 to 4) are the mass densities of H^+, O_2^+, O^+ and CO_2^+, respectively, S_i, and L_i (i=1 to 4) are the mass production and loss rates, respectively, which calculated based on main chemical reactions in the ionosphere including ionization (with rates $\nu_{ph,i}$ and $\nu_{imp,i}$) of each neutral, charge exchange (k_{si}) between the major neutral and ions and recombination reactions(with rates $\alpha_{R,i}$).

Momentum equations for each ion fluid:

$$\rho_i \frac{\partial(\boldsymbol{u}_i)}{\partial t} + \rho_i(\boldsymbol{u}_i \cdot \nabla)\boldsymbol{u}_i$$

$$= -\boldsymbol{\nabla} P_i + \rho_i \boldsymbol{G} + n_i q_i(\boldsymbol{E} + \boldsymbol{u}_i \times \boldsymbol{B}) + \rho_i \sum_{n=neutrals} \nu_{in}(\boldsymbol{u}_n - \boldsymbol{u}_i) + S_i(\boldsymbol{u}_n - \boldsymbol{u}_i) \quad (2)$$

The first three terms on the right-hand side of the momentum equation represent the forces exerted on the plasma, which are ion thermal pressure gradient force, gravity, and electromagnetic forces. The last two terms are ion momentum change due to ion-neutral collisions and chemical reactions, respectively.

The electric field $\boldsymbol{E}$ is defined as

$$\boldsymbol{E} = -\frac{\boldsymbol{\nabla} P_e}{e n_e} - \boldsymbol{u}_e \times \boldsymbol{B} \quad (3)$$

and the electron velocity is given by

$$\boldsymbol{u}_e = \boldsymbol{u}_+ - \frac{\boldsymbol{J}}{e n_e} \quad (4)$$

where $\boldsymbol{u}_+$ is the charge averaged ion velocity.

$$\boldsymbol{u}_+ = \frac{\sum_i n_i q_i \boldsymbol{u}_i}{e n_e} \quad (5)$$

As a result, the electromagnetic forces acting on the plasma (the 3rd item on the right-hand side of equation 2) can be expressed as

$$F_{EMi} = -\frac{n_i \nabla P_e}{n_e} + n_i e(\boldsymbol{u}_i - \boldsymbol{u}_+) \times \boldsymbol{B} + \frac{n_i}{n_e} \boldsymbol{J} \times \boldsymbol{B} \quad (6)$$

The three terms on the right-hand side of the equation (6) correspond to partial electron pressure gradient force, motional electric force and partial $\boldsymbol{J}\times\boldsymbol{B}$ forces. It is important to note that the motional electric force only appears when the ions are moving across the magnetic field. The magnetic field is moving at charge averaged ion velocity (u_+), so the motional electric force on a particular ion depends on its relative velocity to $\boldsymbol{u}_+$. The shocked solar wind protons and planetary ions usually move at different speeds, with the former moving rapidly toward the planet and the latter nearly stationary. So their relative velocity to the charge averaged velocity (that is $\boldsymbol{u_i} - \boldsymbol{u}_+$) are in opposite directions, as a result, solar wind protons and planetary ions "see" the motional electric field with opposite signs [*Dubinin et al*., 2017].

Magnetic induction equation:

$$\frac{\partial \boldsymbol{B}}{\partial t} = \nabla \times (\boldsymbol{u}_e \times \boldsymbol{B} + \frac{\nabla P_e}{e n_e}) \quad (6)$$

The above equation includes the effect of the Hall term, assuming the magnetic field is frozen with electrons and the effect of ambi-polar electric field. The diffusion term in the induction equation is neglected in the model, assuming that the plasma is perfectly conducting. We expect the magnetic diffusion term may be important in the ionosphere below the ionospheric peak region where the plasma is only partially ionized, which will be a subject of future study.

Ion pressure equation for each ion fluid:

$$\frac{\partial P_i}{\partial t} + (\mathbf{u}_i \cdot \nabla) P_i + \gamma P_i (\nabla \cdot \mathbf{u}_i) = \sum_{i=ions} \sum_{n=neutrals} \frac{\rho_i \nu_{in}}{m_i + m_n} [2k(T_n - T_i) + (\gamma - 1) m_n \mathbf{u}_i^{\,2}]$$
$$+ \sum_{i=ions} \nu_{ie} n_i n_e (T_e - T_i) 2k + \frac{(\gamma - 1)}{2} \sum_{i=ions} S_i \mathbf{u}_i^{\,2} + \sum_{i=ions} \left(\frac{S_i T_n - L_i T_i}{m_i} k \right) \quad (7)$$

The pressure of each ion fluid is P_i. The terms on the right-hand side of the equation correspond to the energy exchange due to ion-neutral collisions, ion-electron collisions and chemical reactions (last two terms), respectively.

Electron pressure equation:

$$\frac{\partial P_e}{\partial t} + (\boldsymbol{u_e}\cdot)P_e + \gamma P_e(\nabla\cdot\boldsymbol{u_e}) = \sum_{n=neutrals} \upsilon_{ne} n_n n_e (T_n - T_e) 2k + \sum_{i=ions} \upsilon_{ie} n_i n_e (T_i - T_e) 2k + (\gamma - 1)\sum_{i=ions} N_i \upsilon_{ph,i} E_0 - \sum_{i=ions} n_i \alpha_{R,i} n_e T_e k - L_{e,R(CO2)} - L_{e,V(CO2)} \quad (8)$$

The electron pressure (P_e) is new, relative to the earlier models [*Ma et al.*, 2004; *Najib et al.*, 2011]. The right-hand side terms correspond to the energy exchanges due to electron-neutral collisions, electron-ion collisions, heating due to photo-electrons, recombination reactions respectively. Note that what is calculated here is pressure equation of core thermal electrons, and Te refers to the temperature of thermal electrons. The major heat source for thermal electrons, is Coulomb heating from the suprathermal electron population, while the main energy loss is due to CO_2 collisional rotational and vibrational cooling [*Matta et al.*, 2014; *Sakai et al.*, 2016]. The superthermal electrons heating is included through superthermal photo-electron heating term (the 5th term on the right-hand of Equation 8). E_0 is the approximate heating energy per photo-electron produced due to photoionization process. It is taken to be 1.0 eV in the calculation, estimated based on Sakai et al. [2016]. As for the electron-neutral cooling, we take into account both elastic and inelastic electron-neutral collisions with major neutrals, with the latter including both CO_2 rotational and vibrational cooling processes. The elastic electron-neutral collision rates (ν_{ne}) are taken from Schunk and Nagy [2009], while the CO_2 rotational ($L_{e,R(CO2)}$) and vibrational ($L_{e,V(CO2)}$)energy loss rates are from Dalgarno [1968].

In summary, the improved multi-fluid MHD model solves for the mass density, velocity and pressure of all the four ion fluids, as well as the electron pressure and magnetic field. As in our previous Mars MHD models, the above set of equations is solved using the Michigan BATS-R-US code [*Toth et al.*, 2012], which uses an upwind finite volume scheme, based on the approximate Riemann solver, to ensure the conservation of state variables. In this study, we also used the local time stepping scheme, which allows different grid cells to select different time steps, thereby accelerating convergence and saving computing resources.

The simulation is done in the classic Mars-centered solar orbital (MSO) coordinate system, with the X-axis pointing from Mars to the Sun, and Z-axis perpendicular to Mars orbital plane, and Y-axis completing the right-handed coordinate system, roughly in the direction anti-parallel to the orbital velocity of Mars. The calculation domain covers a broad region of [-24, 8] R_M in X_{MSO} and [-16, 16] R_M in Y_{MSO} and Z_{MSO} directions, where R_M is the radius of Mars (R_M = 3396 km). This large computational domain is used to minimize numerical artifacts from the outer boundary. A non-uniform spherical grid is used with high radial resolution (5 km) near the inner

boundary of 100 km altitude, and gradually increases to 630 km near the downstream outer boundary. The angular resolution is fixed to 3 degrees in both the longitudinal and azimuthal directions throughout the computational domain. The total number of cells is about 2.2 million.

Similar to our previous Mars models [*Ma et al.*, 2004; *Najib et al.*, 2011], the inner boundary of the computation domain is set at 100 km altitude. Because the neutral densities near the inner boundary are very dense, the ion-neutral, electron neutral collisional rates are high, and as a result, the temperature of all the ion fluids and electrons are tightly coupled with the neutral temperature in this collisional dominant region. So, in the model, we set the temperature of all the ion fluids and electrons to be the same as the neutral temperature at the inner boundary ($T_i = T_e = T_n$). At present, the neutral temperature is taken to be a constant at all altitudes in the model, 134K for solar max and 117K for solar min. In addition to set the lower boundary for T_e and T_i, T_n is also used in the ion and electron pressure equations. In the ion pressure equations, it is used to account for ion-neutral collisional cooling effect and for newly generated ions through either ionization or charge exchange processes. In the electron pressure equation, it is used to account for electron-neutral collisional cooling effect. According to MAVEN observations, neutral temperatures are nearly constant or gradually increase with height, especially within the 150–180 km altitude range [*Bougher et al.*, 2017]. Thus, the assumption of a constant T_n will result in a slight underestimation of ion and electron temperatures at high altitudes. The strong ion-neutral collision also results in tight coupling of ions and neutral velocities. The effect of the neutral wind is currently neglected in the model, assuming Un = 0. A reflective boundary condition is applied for the velocities of all ion fluid $(\mathbf{u_i})$ to ensure near zero velocities of all the ion fluids at the inner boundary. The magnetic field vectors are fixed to be the same as the crustal field at the boundary. The crustal field model is taken from *Morschhauser et al.*, [2014], under spring equinox conditions for non-event cases, or the actual configuration for case 4 (see Table 1).

In the current version of the model, the Martian atmosphere consists of three neutrals: CO_2, O and H. For simplicity, we use the same 1D neutral atmospheric profiles for solar max and solar min conditions as used in *Ma et al.* [2004]. The chemical reaction rates are the same as used in *Ma et al.* [2004] and *Najib et al*. [2011]. The only addition is the electron impact ionization, using Brain et al. [2012]. Another improvement of the model is the use of Chapman function instead of cos (SZA) to calculate optical depth [*Ma et al.*, 2015].

To examine the importance of the ambi-polar electric field, we run four cases (see Table 1 for specific parameters used in the run) for three MHD models: multispecies and single-fluid (MS), MF and MFPe. Cases 1-3 are ideal cases, while Case 4 is a MAVEN event study, corresponding to 03 December 2014 (orbit 451). For cases 1-3, the solar wind condition is chosen to be nominal, with a density of 4 cm^{-3}, a velocity of 400 km/s, and thus a dynamic pressure of 1.07 nPa. The IMF follows the typical Parker spiral orientation of 56° at Mars with a magnitude of 3 nT, that is, (B_X, B_Y, B_Z) = (-1.6, 2.5, 0) nT. For case 4, the solar wind density, velocity and the interplanetary magnetic field (IMF) conditions are based on 30 minutes averaged MAVEN Solar Wind Ion Analyzer (SWIA) [*Halekas et al*., 2015] and magnetometer (MAG) [*Connerney et al.*, 2015a]

measurements in the solar wind before the inbound bow shock crossing of the orbit. For cases 1-3, the photo-ionization rates and neutral profiles for solar maximum conditions are used, while for case 4, we used solar minimum conditions to match with the actual EUV condition for the orbit. Also note that for case 1 and case 2, the strong crustal field region is on the dayside and nightside, respectively, while in case 3, the crustal field model is turned off to emphasize the effect of the ambipolar electric field. To directly compare with MAVEN observations, for case 4, the Mars rotation axis is taken to be (-0.416, -0.09, 0.905), and the subsolar latitude and longitude are set to be (131.9, -24.6) degrees to match the actual conditions of Mars at the time when MAVEN was near periapsis on orbit 451.

	Solar EUV conditions	Crustal field	Solar wind density(cm^{-3})	Solar wind velocity(km/s)	IMF(nT)
Case1	Solar max	Yes (dayside)	4	(-400,0,0)	(-1.6,+2.5, 0.0)
Case2	Solar max	Yes (nightside)	4	(-400,0,0)	(-1.6,+2.5, 0.0)
Case3	Solar max	No	4	(-400,0,0)	(-1.6,+2.5, 0.0)
Case4	Solar min	Yes (12-03-2014/08:43 UT)	10.4	(-310,9.3,11.2)	(0.3,-5.6,-1.0)

Table 1. Specific parameters and conditions applied to the cases performed in the study. Solar wind density, velocity and IMF conditions for case 4 are based on SWIA and MAG measurements during the inbound pass of orbit 451.

Section 3. Simulation Results

3.1 Results from the MFPe model

The general interaction patterns, as predicted by the MFPe model, are shown in Figure 1, using case 1 as an example. Across the shock, the plasma flow is slowed down and diverted around the obstacle, while the magnetic field piles up and wraps around, similar to the previous MS and MF model [*Ma et al.*, 2004; *Najib et al.*, 2011]. Keep in mind that for the multi-fluid MHD models, the flow patterns are generally different for different ion fluids, and here the mass-averaged flow is shown. In this case, only the magnetic field contours provide a good indication for the bow shock locations. There is a clear asymmetry in the equatorial (XY) plane, especially for the magnetic field strength due to the IMF direction being the Parker Spiral. The quasi-perpendicular bow shock in the dusk side is slightly farther from the planet, compared with the quasi-parallel shock in the dawn sector, consistent with both MGS and MAVEN observations [*Vignes et al.*, 2001; *Gruesbeck et al.*, 2018]. The bow shock locations also show a clear north-south asymmetry (panel d), with the plasma boundary being slightly farther away from the planet in the southern hemisphere, where the crustal field is relatively strong. The same asymmetry is also observed by MAVEN, as found by *Gruesbeck et al.* [2018], who built a 3D bow shock surface model, using over 1000 MAVEN bow shock crossings. Compared to the previous observations

[*Vignes et al*., 2000; *Trotignon et al*., 2006], both the bow shock positions and the the induced magnetosphere boundary (IMB) positions predicted by the model for case 1 are slightly farther away from the planet. This is because: 1) Case 1 is for solar maximum conditions, and 2) the strong crustal field region faces toward the sun.

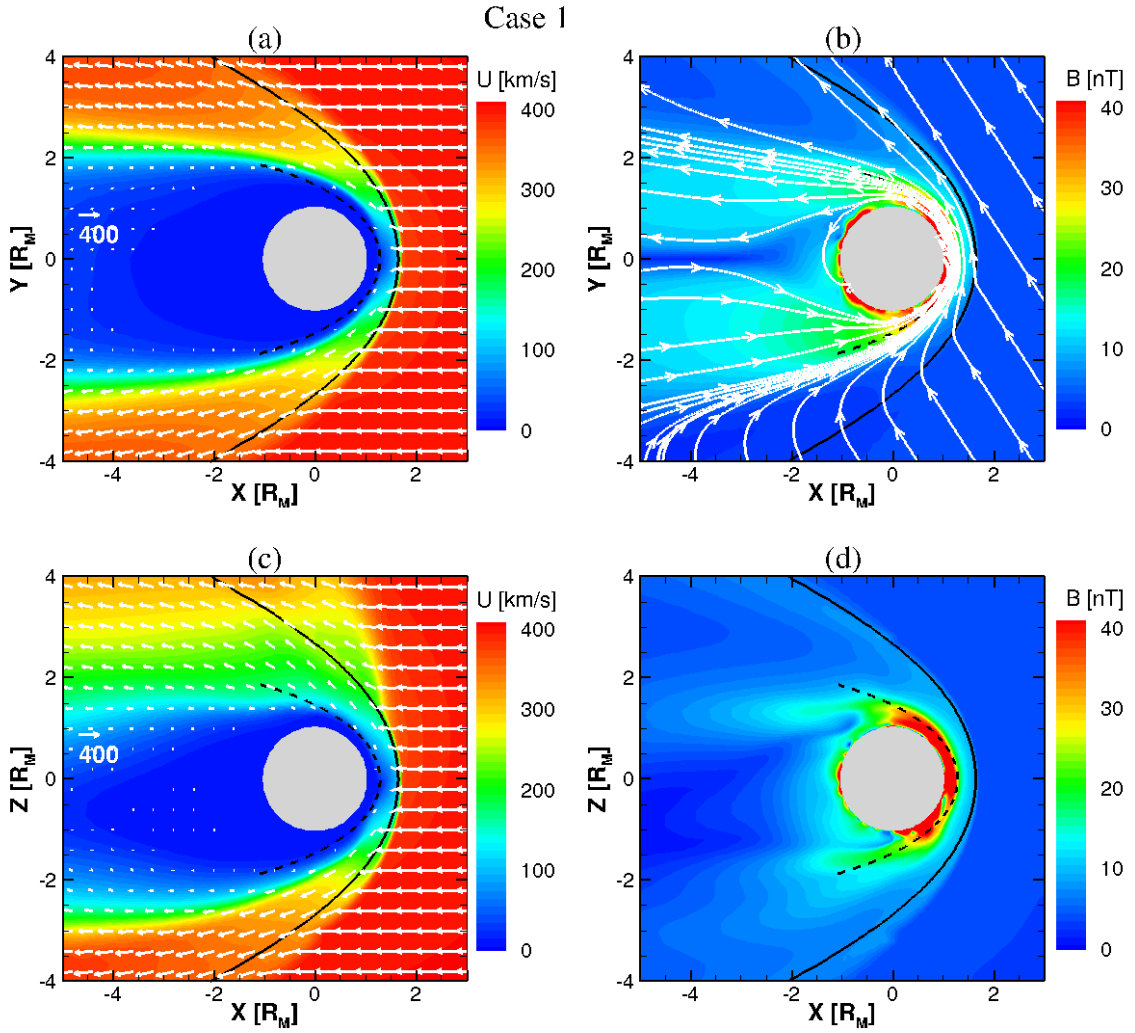

Figure 1. Contour plots of mass-averaged plasma flow speed (left panels) and magnetic field strength (right panels) in the XY plane (a and b) and XZ plane (c and d) for the MFPe model for case 1. The white arrows show the projections of the plasma flow (left panels), and the white lines are projections of magnetic field lines (top right panel). The black solid lines and dashed lines are bow shock and IMB locations, respectively, from Vignes et al. [2000].

For comparison, in Figure 2, we show the model results for the night-side crustal field case (Case 2) and the no crustal field case (Case 3) in the XZ plane in the same format. When the strong crustal field is located at midnight (panel b), the model results match perfectly with the MGS observation of the bow shock and IMB boundaries. When the crustal fields are turned off (panel d), the plasma boundaries, as predicted by the model, are slightly inward as compared with observations most notably near the subsolar region. The subsolar bow shock locations for the three cases are 1.69, 1.61 and 1.54 R_M, respectively, which clearly demonstrate that the presence of crustal fields, especially when located on the dayside, helps to stand off the shocked solar wind.

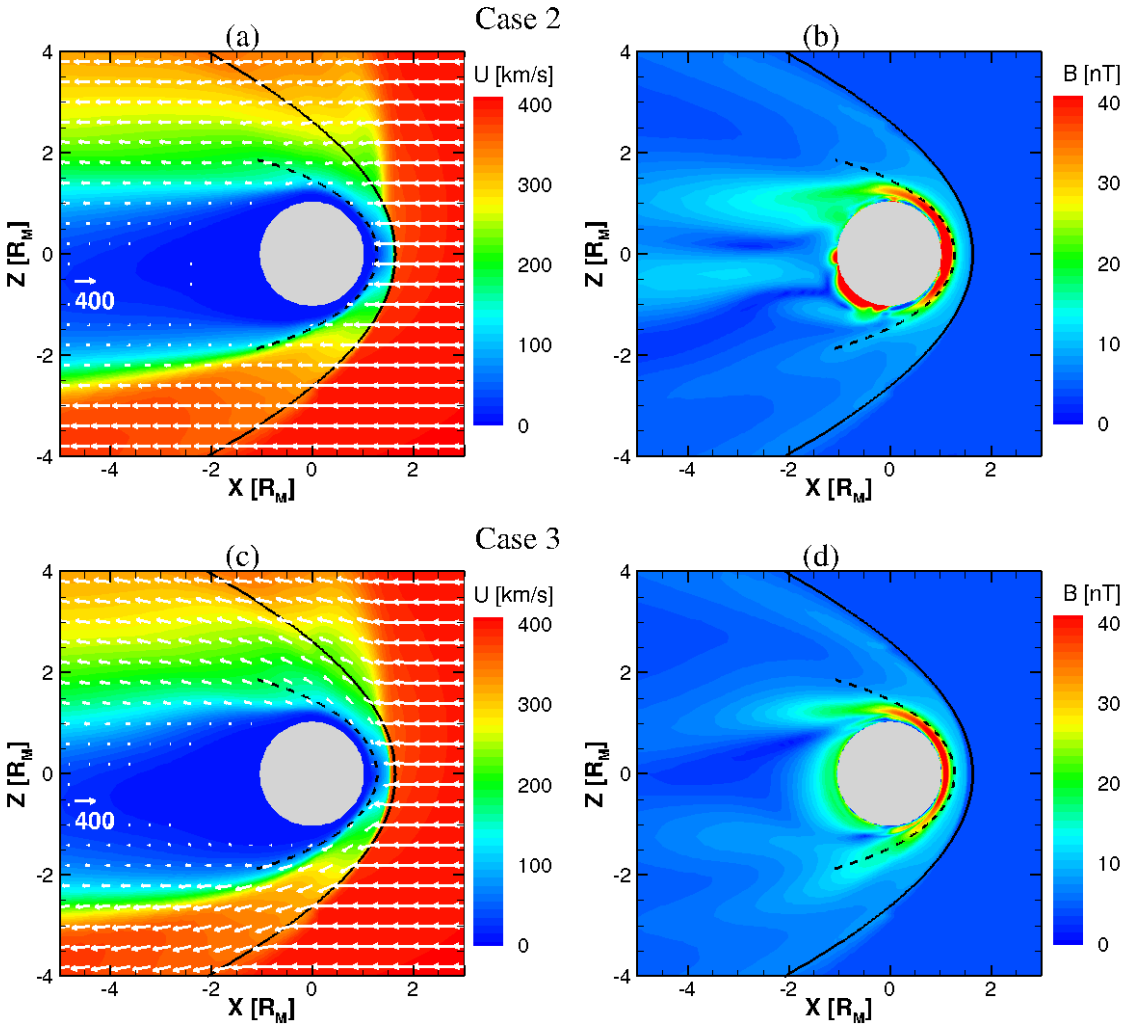

Figure 2. Contour plots of plasma flow speed (left panels) and magnetic field strength (right panels) in the XZ plane for the MFPe model for case 2 (upper panels) and case 3 (bottom panels). The white arrows show the projections of the plasma flow (panels a and c). The black solid lines and dashed lines are bow shock and IMB locations, respectively, from Vignes et al. [2000].

It is also interesting to note that there is a large asymmetry in the XZ plane for all three cases along the convection electric field direction (+Z) for the mass-averaged flow speed (panel c of Figure 1 and panels a and c of Figure 2). This is because, in the current set-up, the convection electric field $\mathbf{E}_{SW} = -(V_{SW} \times B_{IMF})$ aligns with the Z axis in MSO, making the Mars Solar Electric (MSE) coordinates the same as the MSO coordinates. The north-south asymmetry in the flow pattern is caused by the different motional electric field force acting on the plasma (Equation 6), which only arises when different ions move at different flow velocities. This term is especially important in regions where planetary ions and shocked solar wind protons co-exist. As a result, the originally stationary planetary heavy ion fluids are accelerated in the +Z (+E) direction, forming a heavy ion plume as observed by MAVEN [*Dong Y. et al.,* 2015] and as predicted by test particle models [e.g., Fang et al. 2008]. The plume extends in regions even outside of the bow shock in the northern hemisphere, significantly disturbing the solar wind flow. In contrast, the shocked solar wind is accelerated in the opposite direction, and as a result, the plasma wake is shifted slightly downward in the negative Z direction. Similar feature is also observed by MAVEN [*Halekas et al.,* 2018]. It is also worth noting that there is only a small asymmetry of the bow shock locations in the XZ plane for cases 2 and 3 (panels b and d), with the bow shock location being slightly outward in the –Z direction due to the multi-fluid effect caused by motional electric field forces. This clearly demonstrates that the large north-south asymmetry of the bow shock locations in case 1 is mainly caused by the presence of a strong crustal field in the southern hemisphere. This is also consistent with MAVEN results [*Gruesbeck et al*., 2018].

Section 3.2 Comparison of MFPe with MS and MF models

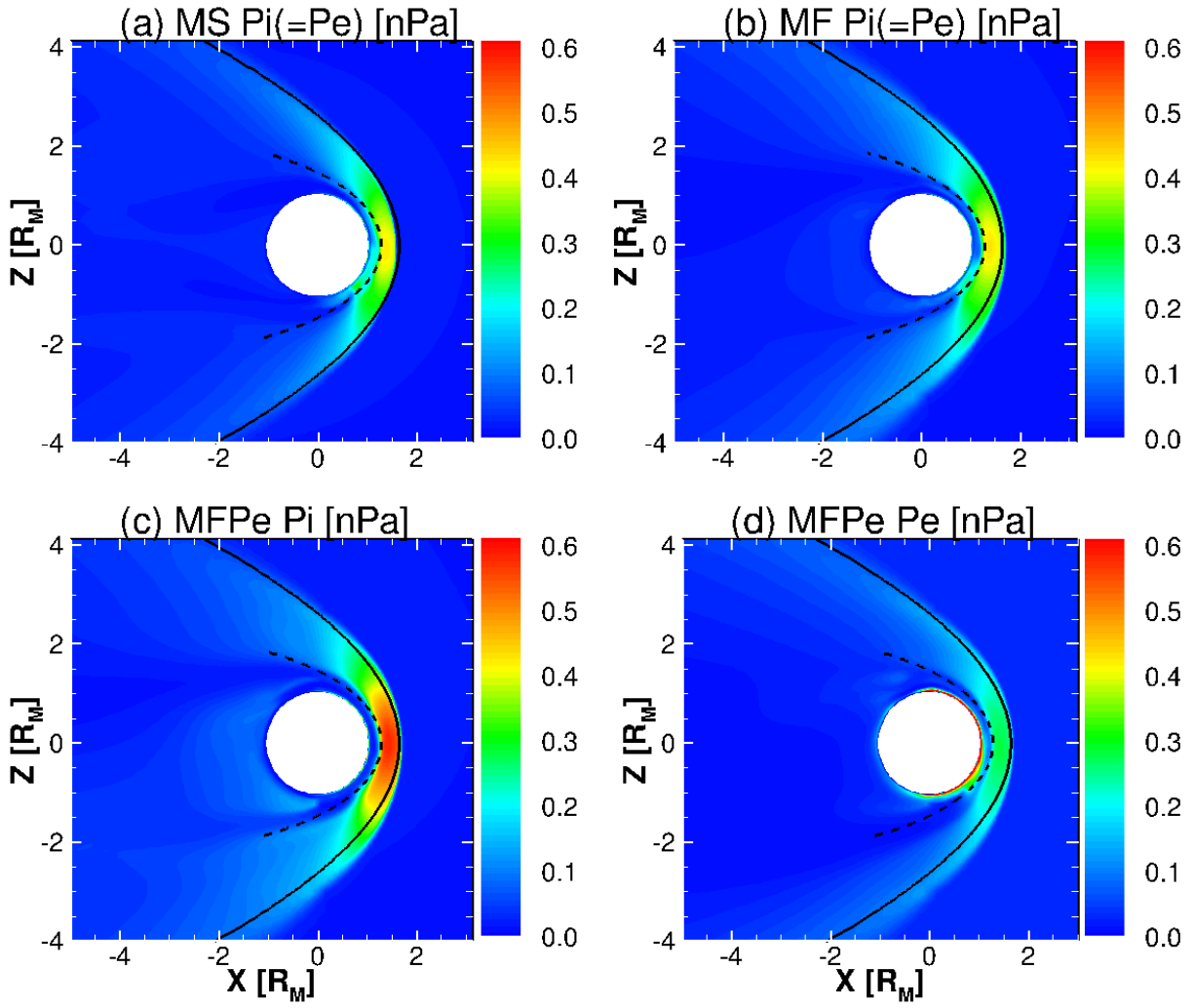

Figure 3. Ion and electron pressure distribution in the XZ plane using MS (multi-species, panel a), MF (Multi-fluid, panel b) and MFPe (multi-fluid with electron pressure equation, panel c and d) models for case 1. The black solid lines and dashed lines are bow shock and IMB locations, respectively, from Vignes et al. [2000].

Figure 3 (and Figure 4) shows a comparison of the ion and electron pressure (and temperature) distributions in the XZ plane using three different models for case 1. Both the MS and MF models solve only ion energy (pressure) equation and assume that the electron pressure (and temperature) are the same as the total ion pressure (and mean ion temperature) (see panels a and b). The MS model results also show some north-south asymmetry in the ionosphere and near the shock, which are mainly due to asymmetric distribution of the crustal fields, but is less apparent

compared with MF and MFPe models. The bow shock location, as predicted by the three models, also varies somewhat. The corresponding subsolar bow shock locations of MS, MF and MFpe models are 1.58, 1.70, and 1.69 R_M, respectively. The large difference between MS and the two MF models clearly show that the multi-fluid treatment results in a relative larger obstacle to the solar wind.

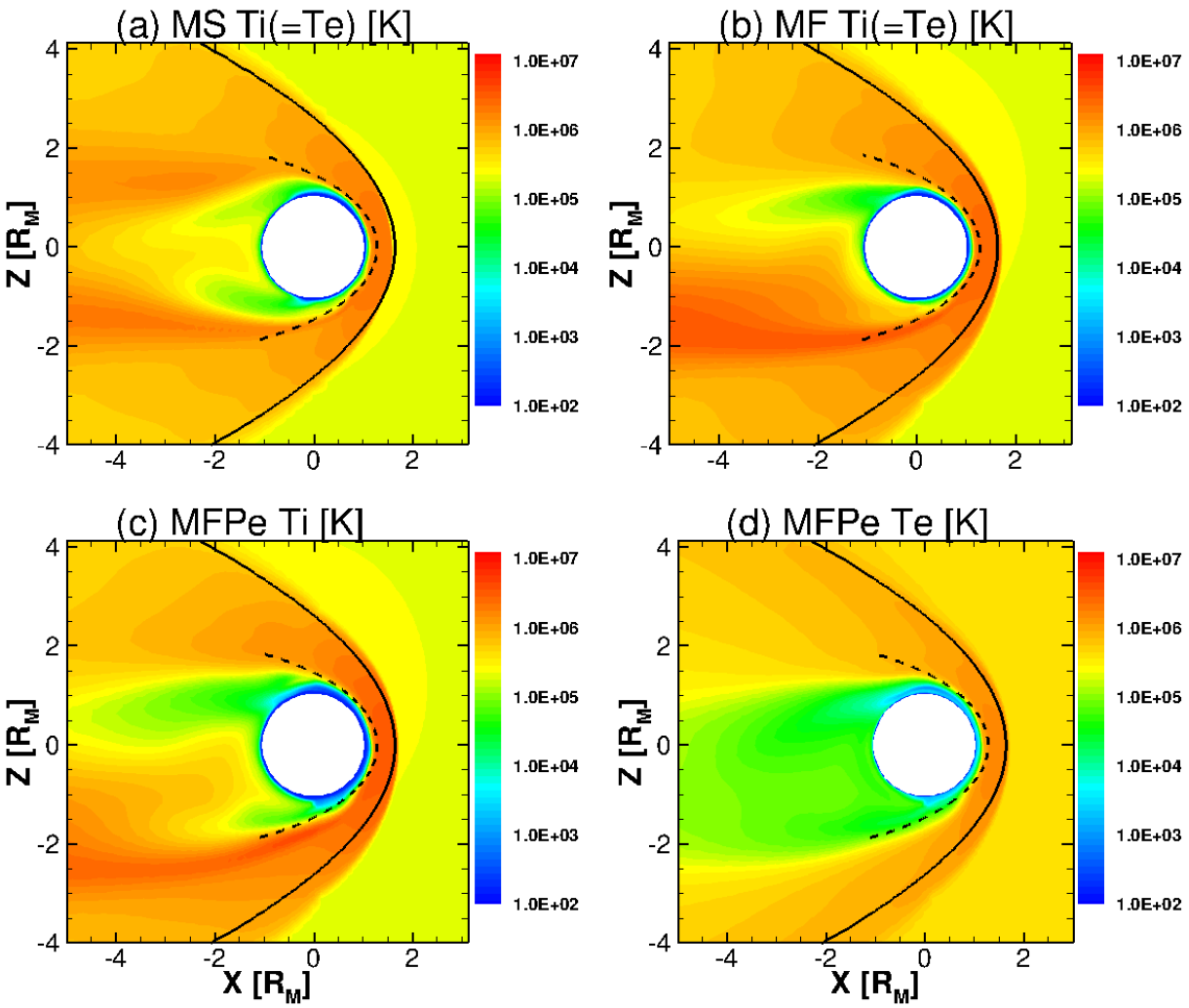

Figure 4. Ion and electron temperature distribution from the three models for case 1, in a format similar to Figure 3.

Because the MFPe model solves the electron pressure equation directly in addition to ion pressure equations, it is the only model that is able to reproduce different ion and electron

pressures (and temperatures) of the three models. As predicted by the MFPe model, the ion and electron temperatures are different in both the ionosphere, where the electron temperatures predominate, and in the magneto-sheath region, where the ion temperatures are relatively high. The pressure (and temperature) distribution in the XY plane are quite symmetric (not shown) for all three models, but show significant asymmetric patterns in the XZ plane due to crustal fields. In addition, regions of strong crustal magnetic field in the dayside feature with higher electron pressure (see panel d of Figure 3), consistent with MAVEN observations [*Flynn et al.*, 2017]. It is worth noting that even though the MFPe model predicts higher electron pressure (temperature) than the MF model in the ionosphere, the two MF models result in very similar bow shock locations.

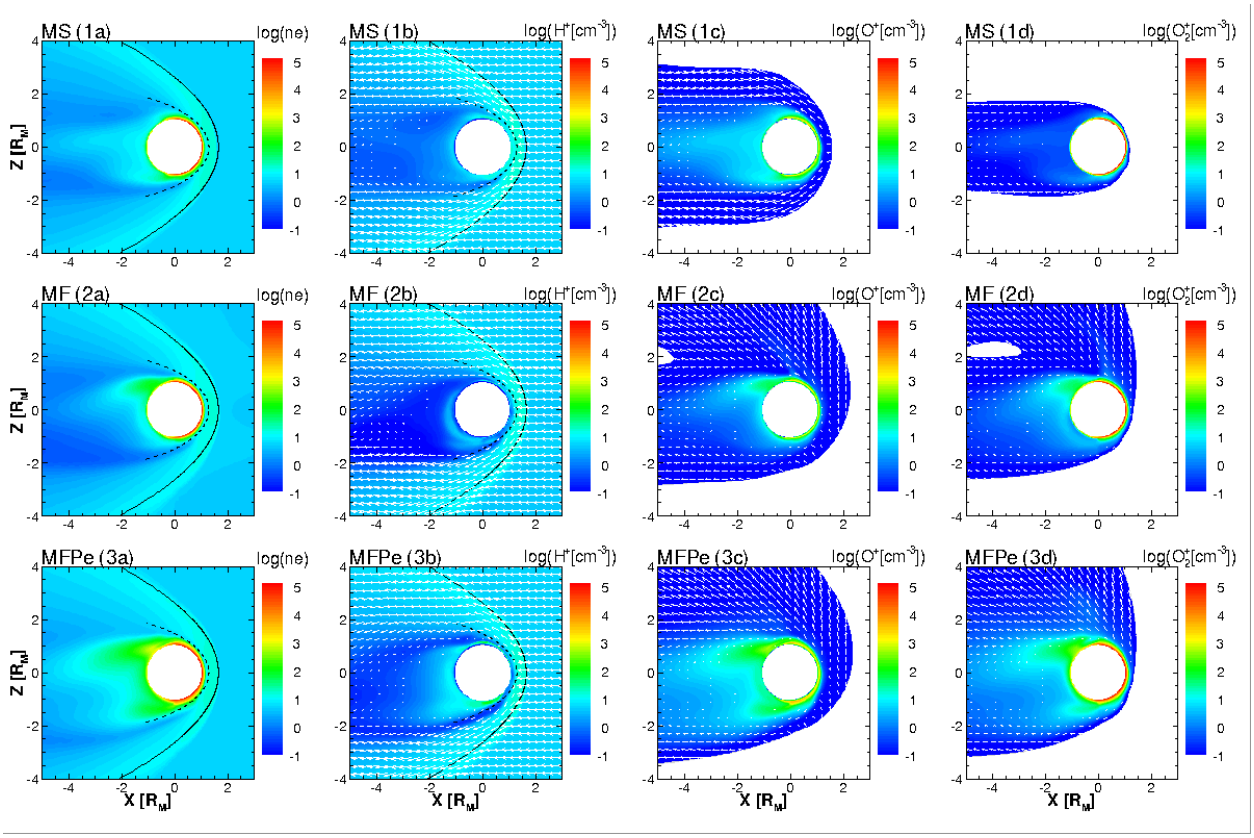

Figure 5. Electron and ion density distributions in the XZ plane using three different models for case 1. The black solid lines and dashed lines are bow shock and IMB locations, respectively, from Vignes et al. [2000]. The white regions are areas where the corresponding densities are less than 0.01 cm^{-3}. The white arrows show flow vectors of corresponding ions.

Figure 5 shows density distributions of electrons and three ions (H^+, O^+, O_2^+) in the XZ plane using three different models for case 1. All the density patterns show clear asymmetric

distribution in north-south direction. The asymmetry in the MS model is the least, which is mainly due to asymmetric crustal field distribution. Both the MF and MFPe models show larger asymmetry, especially for planetary ions (O^+ and O_2^+), with a plume-like structure forming in the northern hemisphere consistent with MAVEN observations [*Dong Y. et al.*, 2015]. The ion plume is formed mainly due to the pick-up process of planetary ions at high altitude, as a result, the densities of heavy ions are largely enhanced in the northern hemisphere (along +E direction). There is also a clearly higher concentration of electrons, O^+ and O_2^+ ion particles in the tail region as predicted by the MFPe model, due to the upwelling of ions in the ionosphere caused by larger electron pressure gradient force (details to be discussed in the next section). Flow vectors are also plotted for each of the three ions, which clearly show that protons have a very different flow pattern, compared to heavy ions (O^+ and O_2^+) for both the MF and MFPe models. The shocked solar wind proton flow diverts around the planet after the shock, while planetary ions are mostly moving along the convection electric field direction, especially in the northern hemisphere.

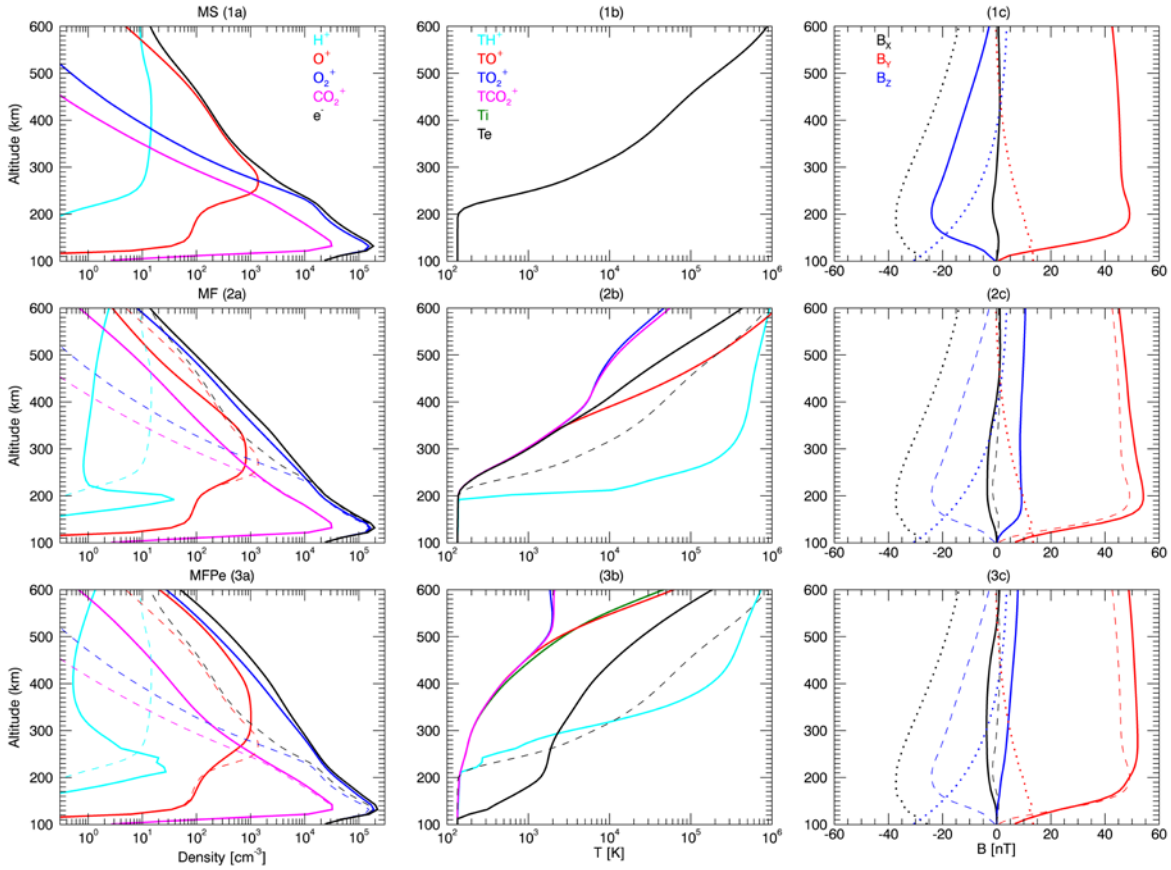

Figure 6. Plasma properties along the subsolar line for MS, MF, and MFpe models for case 1. Results from MS model are also plotted in dashed lines in the middle and lower panels for easy comparison. The solid lines in the right panels show the induced magnetic field, while the dotted lines are the crustal magnetic field (panels 1c, 2c and 3c).

Figure 6 shows altitude profiles of ion and electron densities, and temperatures, as well as magnetic field along the subsolar line for the three different models for case 1. As can be seen from the figure, densities below 200 km are very similar for MS and MF models, as this is below the exobase, a photochemistry dominated region. The densities of the MFPe model differ from the two other models even at low altitude (~ 140 km), especially for O_2^+ and electron densities, due to the fact that some of the chemical reaction rates depend on electron temperature. Below the exobase, both the MS and MF models predict that ion and electron temperatures are about the same as neutral temperature due to the tight coupling between ions and neutrals (note that in panels 1b and 2b, Ti and Te are the same), while Te from the MFPe model is much higher than the neutral temperature because of photo-electron heating (see panel 3b). Given that the dissociative recombination rate of O_2^+ is proportional to $(1/Te)^{0.56}$, with higher electron temperature predicted by the MFPe model, the loss rate of O_2^+ decreases, and the O_2^+ density and the total ion density increase. The peak electron density for the MS and MF models is ~1.85×10^5 cm^{-3}, and for the MFPe model it is 2.21×10^5 cm^{-3}, about 20% higher. The peak altitude of electron densities of all the models remains the same.

At high altitude, the three models differ from each other significantly. Density differences between the MS and the two multi-fluid models (MF and MFPe) result from the decoupling of the velocities of the shocked solar wind proton and planetary ions in the multi-fluid treatment (see in Figure 5 and Figure S1). When we examined the velocity profiles, we found that the proton velocity is very different, compared with the velocities of heavy ions between 200 km and 700 km altitude range for the two multi-fluid models. The MF/MFPe models predict significant acceleration toward the planet of the protons right below the induced magnetosphere boundary, which is likely due to the tension force exerted by the curved magnetic field. Such acceleration is not seen in the MS model, because in the single fluid momentum equation, the ion pressure gradient force counterbalances the magnetic tension force. As the proton flux is roughly a constant, and the charge reactions between H^+ and neutral particles is negligible above exobase, the proton density decreases below IMB in the multi-fluid models due to the acceleration. While the proton density increases rapidly around the exobase (~200 km altitude), as the proton-neutral collision becomes important and significantly slows down the proton flow below the exobase. Both MF and MFPe models predict higher densities of heavy ions at high altitude, due to the ion and electron pressure gradient forces. The MFPe model also predicts higher densities of heavy ions at high altitude than the MF model, due to relatively larger electron pressure gradient force (or ambipolar electric force) in regions between 110 km to 230 km altitude. Also note that ion temperatures at high altitude for the MFPe model is somewhat less than that of the MF model.

This is likely due to the fact that at high altitude, heating of the planetary ions mostly come from the shocked solar wind in the sheath and MPB regions. As the total heat flux from the solar wind is about the same, larger density in the MFPe model results in less heating per ion at high altitude. The major component of the magnetic field in all three models is B_Y, due to draping of the magnetic field. However, there are noticeable differences in B_X and B_Z components in the three models.

3.3 Effect of different forces and current distribution

To better understand the MFPe model results of the flow and field patterns, we also calculated the major forces included in the model. According to the ion momentum equations, five different forces are exerted on each ion fluid: ion pressure gradient force, gravity, partial electron pressure gradient force, and motional electric force and partial $\boldsymbol{J}\times\boldsymbol{B}$ forces. As the gravity force is relatively small compared with the other forces except at very low altitudes, it is neglected in the discussion below. Also, the other forces are all different for different ions. For simplicity, we will sum up the different forces for all the ions and discuss their total effects. Please note that the sum of the motional electric force is zero, so there are only three forces left: ion pressure gradient force, electron pressure gradient force (ambipolar electric field force) and the $\boldsymbol{J}\times\boldsymbol{B}$ force.

We first examine ion and electron pressure gradient forces. The ion and electron pressure forces have a similar effect on the plasma, as shown in Figure 7. Across the shock, both forces dominate with positive X components, and away from subsolar region with substantial positive Y components in the top side and negative Y components in the bottom, meaning that the forces are pointing outward to slow down the solar wind plasma flow. The ion pressure gradient force is somewhat larger than the electron pressure gradient force near the shock. In the magnetosheath region, forces are also dominated by the ion pressure gradient force, mainly in the negative X direction, and away from the subsolar region with negative Y components in the top side and positive Y components in the bottom, compressing the plasma toward the planet. While in the ionosphere, the electron pressure gradient force is the dominant one, which acts together with the ion pressure gradient force to push against the shocked solar wind. The pressure gradient force in the Z direction is negligible near the equatorial plane. The ion pressure gradient force predicted by the model is consistent with that derived from MAVEN plasma observations [*Halekas et al., 2017*].

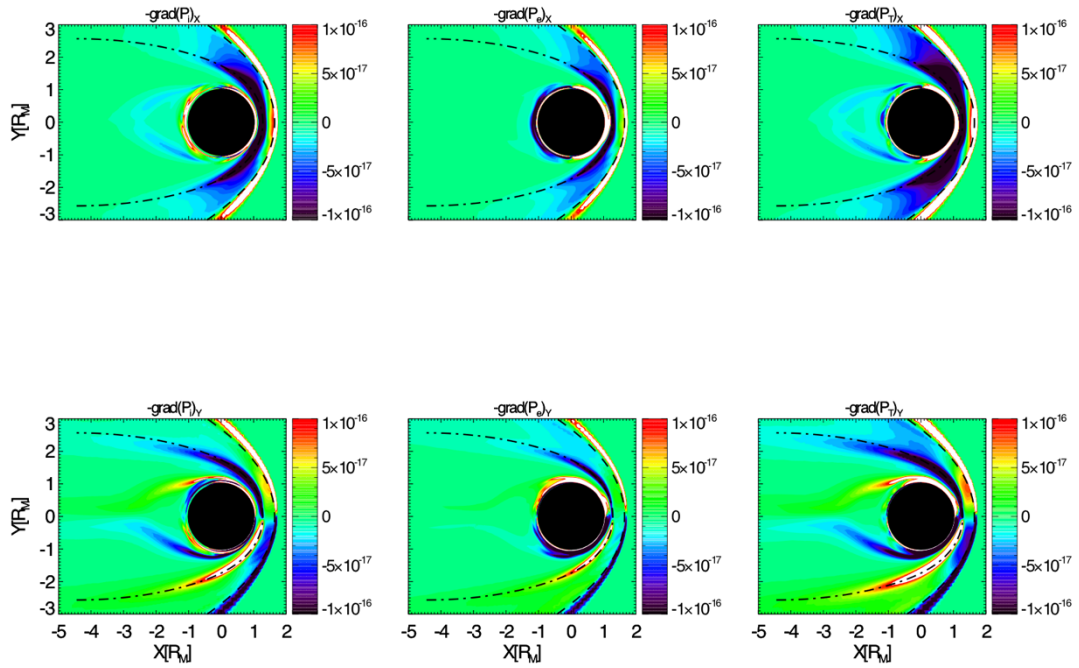

Figure 7. Pressure gradient forces in the X (top panels) and Y direction (bottom panels) for ion, electron and total pressure in the equatorial (XY) plane for the MFPe model for case 1.

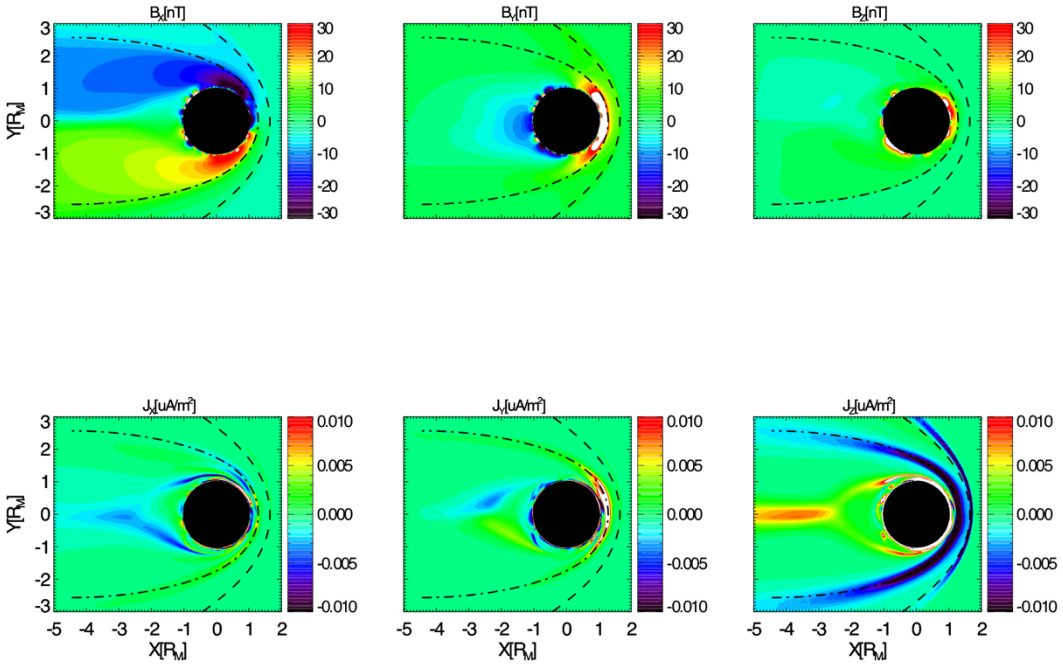

Figure 8. Magnetic field components and current system in the equatorial (XY) plane for the MFPe model for case 1.

Figure 8 shows the three components of the total magnetic field (top panels) and electric current (bottom panels) formed around Mars due to plasma interaction in the equatorial plane. The total magnetic field is the sum of the crustal field and induced magnetic field (or perturbations of the magnetic field). Except in regions very close to the planet, magnetic field is dominated by the induced magnetic field. The magnetic field pattern is consistent with the draping pattern observed by MGS [*Crider et al.*, 2004] and MAVEN [*Connerney et al.*, 2015b; *Halekas et al.*, 2017]. The B_X component shows a clear bipolar signature, and there is significant enhancement of the B_Y component inside the IMB due to the slowdown of the solar wind plasma flow. The B_Z component is relatively small in most regions, except close to the planet, due to the presence of localized crustal magnetic fields.

The electric current is calculated using the curvature of the magnetic field. As shown in Figure 8 (bottom right panel), the currents are mainly flowing in the Z direction. They are mainly distributed in four regions: bow shock, induced magnetosphere, ionosphere, and tail current sheet. The currents are flowing in a negative Z direction, near the bow shock and inside the induced magnetosphere, meaning that they both enhance the B_Y component. The currents induced in the ionosphere and the tail region are flowing in the opposite direction. As the ionosphere is a a highly conducting region, the main effect of the current induced in the ionosphere is to counter

the penetration of the magnetic field to lower altitude. The tail current sheet is formed due to the draping of the magnetic field lines (see upper left panel of Figure 8).

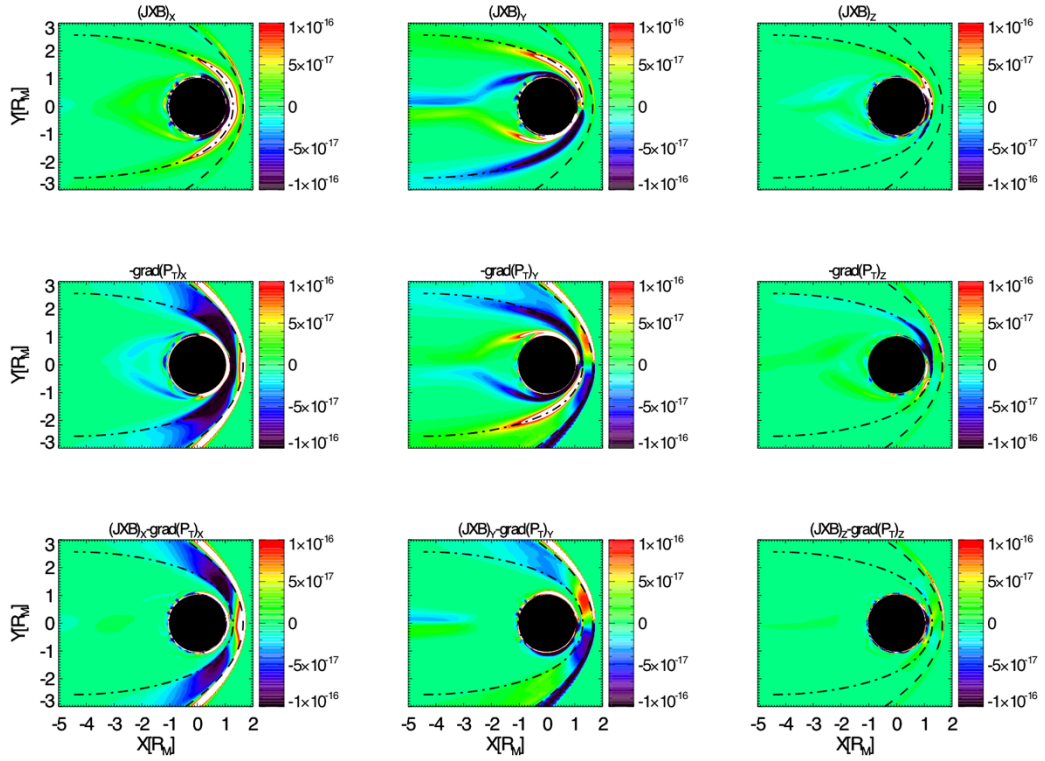

*Figure 9. 2D plot of the **J**×**B** force (top panels) and total pressure gradient force (middle panels) and the total of the two forces (bottom panels) in three directions in the equatorial (XY) plane for the MFPe model for case 1.*

The ***J***×***B*** force, total (ion + electron) pressure gradient force, and their sum are shown in Figure 9. Near the shock, the ***J***×***B*** force is in the same direction as the total pressure gradient force, and they act together to slow down the plasma across the bow shock. However, inside the induced magnetosphere, the ***J***×***B*** force is pointing outward, opposite to the total pressure gradient force, and the two forces roughly cancel each other out near the subsolar region. The net force of the two diverts the shocked solar wind around the obstacle. The ***J***×***B*** force patterns predicted by the model are also consistent with MAVEN observations [*Halekas et al.,* 2017].

Section 3.4 Comparison with MAVEN observations

We also conducted a case study using the three models in order to show their differences as well as how they compare with plasma observations. The case study is for 13 December 2014, orbit 451. The solar wind condition during this time period is relatively quiet. We first calculated the

average solar wind condition using SWIA measurements before the inbound bow shock crossings and used that as the input parameters of the model runs, as listed in Table 1 for case 4.

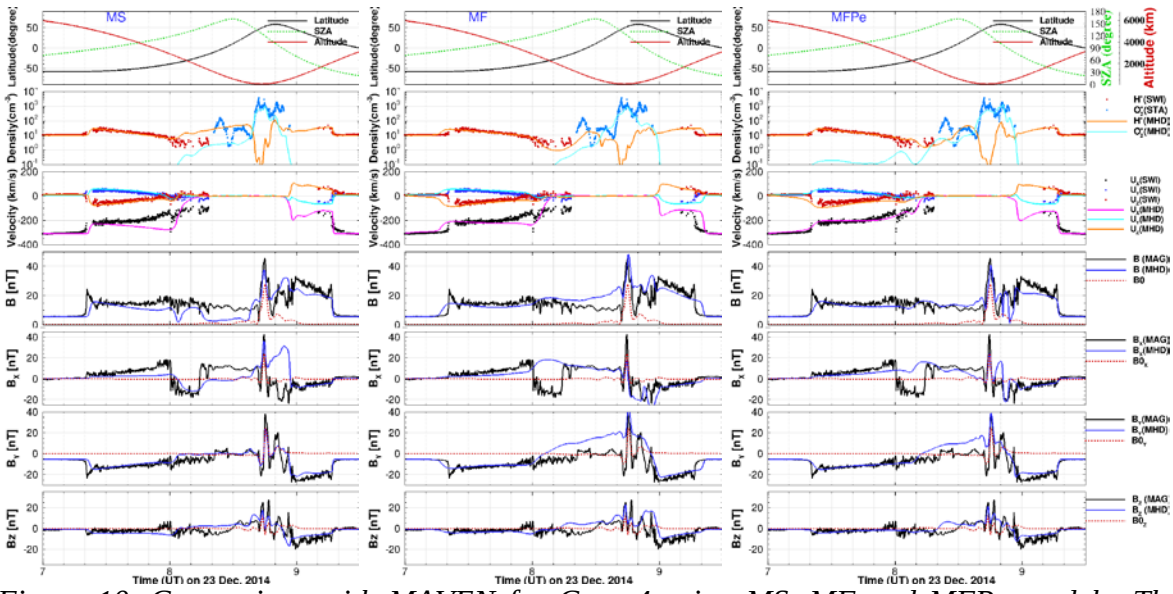

Figure 10. Comparison with MAVEN for Case 4 using MS, MF and MFPe models. The first panel in each case show MAVEN trajectory information (latidue, SZA and altitude). Second panel compares MHD model results with proton density observed by SWIA and O_2^+ density observed by STATIC. Third panel compares model results with plasma velocity vectors as observed by SWIA. The last four panels compare model results with MAG observations for the strength and the three components of the magnetic fields.

Figure 10 shows the data-model comparison using three MHD models. As shown, the O_2^+ density profiles near periapsis are all well reproduced by the three models. But the second peak of O_2^+ density during the outbound trajectory is best reproduced by the MFPe model. The MFPe model also agrees the best with O_2^+ density at high altitude.

The three models predict slightly different locations of the bow shock, and the observed shock locations for both inbound and outbound passes are best reproduced by the MFPe model. The U_Y and U_Z profiles by all three models match well with SWIA observations, but for the U_X component, the MFPe model results agree best with SWIA observations. As for the magnetic field, there are some discrepancies in all three components and field magnitude for all three models, which are likely due to the fact that the IMF condition is highly variable, while such variations of the IMF are neglected in the steady-state runs. In comparison, the B_Y component agrees best with the MS model, but the observed magnitude of the field is best matched by the MFPe model. In general, we find the that MFPe model matches best with the relevant MAVEN plasma observations. We did not compare model results with Te measured by the LPW

instrument, because no LPW data is available for this particular orbit. But the electron temperature in Figure 6(3b) are qualitatively similar to MAVEN LPW observations as shown in *Ergun et al.* [2015]. More direct comparison with LP measurements will be done in future work.

Section 3.5 Escape rates

	Model	$O^+(\times10^{24}/s)$	$O_2^+(\times10^{24}/s)$	$CO_2^+(\times10^{24}/s)$	Total number $(\times10^{24}/s)$	Total mass (kg/s)
Case 1 (with B0 dayside)	MS	3.97	0.25	0.03	4.25	0.12
	MF	3.30	1.97	0.25	5.53	0.21
	MFpe	5.74	3.34	0.07	9.15	0.34
Case 2 (with B0 night-side)	MS	4.37	0.17	0.02	4.55	0.13
	MF	5.19	2.26	0.23	7.67	0.28
	MFpe	7.89	4.72	0.04	12.6	0.47
Case 3 (no crustal field)	MS	6.72	0.67	0.06	7.45	0.22
	MF	5.98	1.32	0.18	7.49	0.25
	MFpe	6.95	3.21	0.13	10.3	0.37
Case 4 (MAVEN case study)	MS	1.67	0.39	0.03	2.09	0.07
	MF	1.26	0.69	0.09	2.04	0.08
	MFpe	1.08	2.27	0.14	3.49	0.16

Table 2. Escape rates for the four cases with three different models.

We also examined ion escape rates for all the cases. The ion escape rates are integrated through the 6 R_M spherical surface. The results are listed in Table 2. The total escape rates of the MF models are generally similar or larger than the corresponding MS model results. However, the main escaping ions, as predicted by the two MF models, are different. The MF model predicts that more heavy ions (O_2^+ and CO_2^+) are lost from the planet, while the MS model favors the loss of the light O^+ ions. The escape rates predicted by the MFPe model are the highest, especially for heavy ions. The total escape rates increased by 38%-177% percent when using the MFPe model, as compared with corresponding MS model results in total number density, which corresponds to 67%- 265% increase in total mass loss. Compared with corresponding MF model results, the increase is between 37-71% in total number density, and 50-108% in total mass loss. Also, it is interesting to compare different cases. Comparison between Cases 1 and 2 show the effect of crustal field orientation on the total ion loss rates. All three models predict lower total ion loss rates when the strong crustal field is facing toward the Sun. However, when comparing case 2 and case 3, we found that both the MS and MF models predict that the escape rates are the largest when the crustal field is turned off, while for MFPe model, the escape rates for case 3 are actually smaller than those of case 2, meaning that under some weak crustal field configurations,

when taking into account the ambipolar electric field, the ion escape rates could be larger than without crustal field. Also note that cases 1-3 are for solar max. For case 4, the MAVEN event case, we are using solar minimum conditions, so the escape rates are the smallest of the four cases, indicating that solar EUV is one of the main factors controlling the total ion loss rate.
The total ion loss rates predicted by the MFPe model for the 4 cases are between 3.5×10^{24} $s^{-1}$to 1.3×10^{25} s^{-1}, much larger than previous MS and MF model predictions, which clearly demonstrated the importance of ambipolar electric field in driving ion loss from Mars. The predicted ion loss rates by the new model are in the same range as the estimated escape rates between 2×10^{24} to 3×10^{25} s^{-1} when the low energy ions are included using Phobos and MEX data at different times [*Lundin et al.*,1990, 2008; *Fränz et al*.,2010; *Nilsson et al.*, 2011; *Ramstad et al*., 2013]. The new model results are also consistent with theoretical predictions [*Cravens et al.*, 2017].

Section 4. Summary and discussion

The multi-fluid (MF) magnetohydrodynamic (MHD) model of Mars is improved by solving an additional electron energy equation. With the electron energy equation, the electron temperature is calculated based on the effects from various electron-related heating and cooling processes (e.g. photo-electron heating, electron-neutral collision and electron-ion collision), and thus the improved model is able to calculate the electron temperature and the electron pressure force terms self-consistently. The general interaction patterns, as predicted by the MFPe model, are similar to those of the MF model. Comparison of the first three cases clearly showed that the presence of the crustal fields, especially when located on the dayside, helps to stand off the shocked solar wind, consistent with MAVEN observations.

Model results of a typical case using the MFPe are compared in detail to both MS and MF models with identical input conditions to identify the effect of the improved physics. The model with electron pressure equation predicts that the electron temperature is much larger than the ion temperature in the ionosphere, consistent with both Viking and MAVEN observations.

Different plasma forces act together during the interaction process. We compared the major forces considered in the MHD model: the ion and electron pressure gradient forces and the $\boldsymbol{J}\times\boldsymbol{B}$ $\boldsymbol{B}$ force. Using our numerical model, we also examined in detail the relative importance of different forces in the plasma interaction region. Across the shock, the ion pressure gradient force is the main force to slow down the solar wind. In the induced magnetosphere, the ion pressure gradient force and the $\boldsymbol{J}\times\boldsymbol{B}$ force counterbalance each other in the subsolar region. While in the ionosphere, the electron pressure gradient force is the dominant one.

All three models are applied to a MAVEN event study using identical input conditions derived from MAVEN observations. The improved MFPe model matches best with MAVEN

observations. Finally, the ion escape rates are calculated for all the cases, and we found that the inclusion of the electron pressure equation increases the escape rates predicted by the model by 50%-110% in total mass, compared with MF model, which clearly demonstrates the importance of the ambipolar electric field.

Acknowledgments: This work was supported by NASA grant NNH10CC04C to the University of Colorado and by subcontract to UCLA. The MAVEN project is supported by NASA through the Mars Exploration Program. The MAVEN data used in this study are available through Planetary Data System (http://ppi.pds.nasa.gov/mission/MAVEN). The BATS-R-US code is publicly available from http://csem.engin.umich.edu/tools/swmf.

References:

Acuña, M. H., et al. (1998). Magnetic field and plasma observations at Mars: Initial results of the Mars Global Surveyor Mission. Science, 279, 1676–1680. https://doi.org/10.1126/science.279.5357.1676

Acuña, M. H., et al. (1999), Global distribution of crustal magnetization discovered by the Mars Global Surveyor MAG/ER experiment, *Science*, **284**, 790–793.

Axford, W. I. (1968), The polar wind and the terrestrial helium budget, J. Geophys. Res., 73(21), 6855– 6859, doi:10.1029/JA073i021p06855.

Banks, P. M., and Holzer, T. E. (1968), The polar wind, J. Geophys. Res., 73(21), 6846– 6854, doi:10.1029/JA073i021p06846.

Barabash, S., et al. (2007), Martian atmospheric erosion rates, Science, 315, 501, doi:10.1126/science.1134358.

Bertucci, C., Duru, F., Edberg, N. et al., The Induced Magnetospheres of Mars, Venus, and Titan**,** Space Sci Rev (2011) 162: 113. https://doi.org/10.1007/s11214-011-9845-1

Bougher, S. W., et al. (2017), The structure and variability of Mars dayside thermosphere from MAVEN NGIMS and IUVS measurements: Seasonal and solar activity trends in scale heights and temperatures, *J. Geophys. Res. Space Physics*, 122, 1296– 1313, doi:10.1002/2016JA023454.

Brain, D.A., (2006), Mars Global Surveyor measurements of the Martian solar wind interaction, Space Sci. Rev. 126 (January), 77–112. doi:10.1007/s11214-006-9122-x.

Brecht, S. H., Ledvina, S. A., and Bougher, S. W. (2016), Ionospheric loss from Mars as predicted by hybrid particle simulations, *J. Geophys. Res. Space Physics*, 121, 10,190– 10,208, doi:10.1002/2016JA022548.

Brecht, S. H., and S. A. Ledvina (2014), The role of the Martian crustal magnetic fields in controlling ionospheric loss, *Geophys. Res. Lett.*, **41**, 5340–5346, doi:10.1002/2014GL060841.

Brecht, S. H. and S. A. Ledvina (2010), The loss of water from Mars: Numerical results and challenges, *Icarus*, **206**(1), 164–173, doi:10.1016/j.Icarus.2009.04.028.

Collinson, G., Mitchell, D., Glocer, A., Grebowsky, J., Peterson, W. K., Connerney, J., Andersson, L., Espley, J., Mazelle, C., Sauvaud, J.-A., Fedorov, A., Ma, Y., Bougher, S., Lillis, R., Ergun, R., & Jakosky, B. (2015). Electric Mars: The first direct measurement of an upper limit for the Martian "polar wind" electric potential. Geophysical Research Letters, 42, 9128– 9134. https://doi.org/10.1002/2015GL065084

Collinson, G., Mitchell, D., Xu, S., Glocer, A., Grebowsky, J., Hara, T., et al. (2016). Electric Mars: A large trans-terminator electric potential drop on closed magnetic field lines above Utopia Planitia. Journal of Geophysical Research: Space Physics, 122, 2260– 2271. https://doi.org/10.1002/2016JA023589

Collinson, G., Glocer, A., Xu, S., Mitchell, D. L., Frahm, R. A., Grebowsky, J., et al. (2019). Ionospheric ambipolar electric fields of Mars and Venus: Comparisons between theoretical predictions and direct observations of the electric potential drop. Geophysical Research Letters, 46, 1168– 1176. https://doi.org/10.1029/2018GL080597

Connerney, J.E.P., Espley, J.R., Lawton, P., Murphy, S., Odom, J., Oliversen, R., & Sheppard, D. (2015a). The MAVEN magnetic field investigation. *Space Sci. Rev.*, vol. 195, no. 1, pp. 257-291, doi: 10.1007/s11214-015-0169-4

Connerney, J. E. P., Espley, J. R., DiBraccio, G. A., Gruesbeck, J. R., Oliversen, R. J., Mitchell, D. L., … Jakosky, B. M. (2015b). First results of the MAVEN magnetic field investigation. Geophysical Research Letters, 42, 8819–8827. https://doi.org/10.1002/2015GL065366

Cravens, T. E., Hamil, O., Houston, S., Bougher, S., Ma, Y., Brain, D. & Ledvina, S. (2017). Estimates of ionospheric transport and ion loss at Mars. *Journal of Geophysical Research: Space Physics*, 122, 10,626– 10,637. https://doi.org/10.1002/2017JA024582

Crider, D., Brain, D. A., Acuña, M., Vignes, D., Mazelle, C., & Bertucci, C. (2004). Mars Global Surveyor observations of solar wind magnetic field draping around Mars. Space Science Reviews, 111(1/2), 203–221. https://doi.org/10.1023/B:SPAC.0000032714.66124.4e

Dong, C., Bougher, S. W., Ma, Y., Toth, G., Lee, Y., Nagy, A. F., Tenishev, V., Pawlowski, D. J., Combi, M. R., and Najib, D. (2015), Solar wind interaction with the Martian upper

atmosphere: Crustal field orientation, solar cycle, and seasonal variations, *J. Geophys. Res. Space Physics*, 120, 7857– 7872, doi:10.1002/2015JA020990.

Dong, Y., Fang, X., Brain, D. A., McFadden, J. P., Halekas, J. S., Connerney, J. E., Curry, S. M., Harada, Y., Luhmann, J. G., and Jakosky, B. M. (2015), Strong plume fluxes at Mars observed by MAVEN: An important planetary ion escape channel, *Geophys. Res. Lett.*, 42, 8942– 8950, doi:10.1002/2015GL065346.

Dubinin, E., Fraenz, M., Pätzold, M., Halekas, J. S., Mcfadden, J., Connerney, J. E. P., et al. (2018). Solar wind deflection by mass loading in the Martian magnetosheath based on MAVEN observations. *Geophysical Research Letters*, 45, 2574– 2579. https://doi.org/10.1002/2017GL076813

Edberg, N. J. T., Lester, M., Cowley, S. W. H., and Eriksson, A. I. (2008), Statistical analysis of the location of the Martian magnetic pileup boundary and bow shock and the influence of crustal magnetic fields, *J. Geophys. Res.*, 113, A08206, doi:10.1029/2008JA013096.

Ergun, R. E., Morooka, M. W., Andersson, L. A., Fowler, C. M., Delory, G. T., Andrews, D. J., Eriksson, A. I., McEnulty, T., and Jakosky, B. M. (2015), Dayside electron temperature and density profiles at Mars: First results from the MAVEN Langmuir probe and waves instrument, *Geophys. Res. Lett.*, 42, 8846– 8853, doi:10.1002/2015GL065280.

Ergun, R. E., et al. (2016), Enhanced O_2^+ loss at Mars due to an ambipolar electric field from electron heating, *J. Geophys. Res. Space Physics*, 121, 4668–4678, doi: 10.1002/2016JA022349. https://doi.org/10.1002/2016JA022349

Fang, X., M. W. Liemohn, A. F. Nagy, Y. Ma, D. L. De Zeeuw, J. U. Kozyra, and T. H. Zurbuchen (2008), Pickup oxygen ion velocity space and spatial distribution around Mars, J. Geophys. Res., 113, A02210, doi:10.1029/2007JA012736.

Flynn, C. L., Vogt, M. F., Withers, P., Andersson, L., England, S., & Liu, G. (2017). MAVEN observations of the effects of crustal magnetic fields on electron density and temperature in the Martian dayside ionosphere. *Geophysical Research: Letters*, 44, 10,812– 10,821. https://doi.org/10.1002/2017GL075367

Fränz, M., E. Dubinin, E. Nielsen, J. Woch, S. Barabash, R. Lundin, and A. Fedorov(2010), Transterminator ion flow in the Martian ionosphere, *Planet. Space Sci.*, **58**(1), 1442–1454, doi:10.1016/j.pss.2010.06.009.

Ganguli, S. B. (1996). The polar wind. Reviews of Geophysics, 34(3), 311– 348. https://doi.org/10.1029/96RG00497

Glocer, A., Khazanov, G., and Liemohn, M. (2017). Photoelectrons in the quiet polar wind. Journal of Geophysical Research: Space Physics, 122, 6708–6726. https://doi.org/10.1002/2017JA024177

Gruesbeck, J. R., Espley, J. R., Connerney, J. E. P., DiBraccio, G. A., Soobiah Y. I., D. Brain, et al. (2018). The three-dimensional bow shock of Mars as observed by MAVEN. Journal of Geophysical Research: Space Physics, 123. https://doi.org/10.1029/2018JA025366

Halekas, J., E. Taylor, G. Dalton, G. Johnson, D. Curtis, J. McFadden, D. Mitchell, R. Lin, and B. Jakosky (2015), The solar wind ion analyzer for MAVEN, *Space Sci. Rev.*, **195**, 125–151, doi:10.1007/s11214-013-0029-z

Halekas, J. S., Brain, D. A., Luhmann, J. G., DiBraccio, G. A., Ruhunusiri, S., Harada, Y., … Jakosky, B. M. (2017). Flows, fields, and forces in the Mars-solar wind interaction. *Journal of Geophysical Research: Space Physics*, 122, 11,320–11,341. https://doi.org/10.1002/2017JA024772

Halekas, J. S., McFadden, J. P., Brain, D. A., Luhmann, J. G., DiBraccio, G. A., Connerney, J. E. P., et al. (2018). Structure and variability of the Martian ion composition boundary layer. *Journal of Geophysical Research: Space Physics*, 123, 8439–8458. https://doi.org/10.1029/2018JA025866

Jakosky, B. M., Lin, R., Grebowsky, J., Luhmann, J., Mitchell, D., Beutelschies, G., et al. (2015). The Mars Atmosphere and Volatile EvolutioN (MAVEN) mission. Space Science Reviews, 195(1-4), 3– 48.

Kallio, E., K. Liu, R. Jarvinen, V. Pohjola, and P. Janhunen(2010), Oxygen ion escape at Mars in a hybrid model: High energy and low energy ions, *Icarus*, **206**, 152–163, doi:10.1016/j.icarus.2009.05.015.

Lillis, R. J., Halekas, J., Fillingim, M., Poppe, A., Collinson, G., Brain, D. A., & Mitchell, D. (2018). Field-aligned electrostatic potentials above the Martian exobase from MGS electron reflectometry: Structure and variability. Journal of Geophysical Research: Planets, 123, 67–92. https://doi.org/10.1002/2017JE005395

Lundin, R., A. Zakharov, R. Pellinen, S. W. Barabasj, H. Borg, E. M. Dubinin, B. Hultqvist, H. Koskinen, I. Liede, and N. Pissarenko (1990), ASPERA/Phobos measurements of the ion

outflow from the Martian ionosphere, *Geophys. Res. Lett.*, **17**, 873–876, doi:10.1029/GL017i006p00873.

Lundin, R., S. Barabash, M. Holmström, H. Nilsson, M. Yamauchi, M. Fraenz, and E. M. Dubini (2008), A comet-like escape of ionospheric plasma from Mars, *Geophys. Res. Lett.*, **35**, L18203, doi:10.1029/2008GL034811.

Ma, Y., A. F. Nagy, I. V. Sokolov, and K. C. Hansen (2004), Three-dimensional, multispecies, high spatial resolution MHD studies of the solar wind interaction with Mars, J. Geophys. Res., 109, A07211, doi:10.1029/2003JA010367.

Ma, Y. J., et al. (2011), The importance of thermal electron heating in Titan's ionosphere: Comparison with Cassini T34 flyby, *J. Geophys. Res.*, 116, A10213, doi:10.1029/2011JA016657.

Ma, Y. J., et al. (2015), MHD model results of solar wind interaction with Mars and comparison with MAVEN plasma observations, Geophys. Res. Lett., 42, 9113–9120, doi:10.1002/2015GL065218.

McFadden, J., Kortmann, O., Curtis, D., Dalton, G., Johnson, G., Abiad, R., et al. (2015). MAVEN SupraThermal And Thermal Ion Composition (STATIC) instrument. Space Science Reviews, 195(1-4), 199– 256.

Mitchell, D. L., Lin, R. P., Mazelle, C., Rème, H., Cloutier, P. A., Connerney, J. E. P., Acuña, M. H. and Ness, N. F.: 2001, 'Probing Mars' Crustal Magnetic Field and Ionosphere with the MGS Electron Reflectometer', J. Geophys. Res. 106, 23419.

Mitchell, D., Mazelle, C., Sauvaud, J.-A., Thocaven, J.-J., Rouzaud, J., Fedorov, A., et al. (2016). The MAVEN Solar Wind Electron Analyzer. Space Science Reviews, 200(1-4), 495– 528.

Moore, T. E., Chappell, C. R., Chandler, M. O., Craven, P. D., Giles, B. L., Pollock, C. J., Burch, J. L., Young, D. T., Waite, J. H. Jr., Nordholt, J. E., Thomsen, M. F., McComas, D. J., Berthelier, J. J., Williamson, W. S., Robson, R., & Mozer, F. S. (1997). High-altitude observations of the polar wind. Science, 277, 349– 351.

Modolo, R., Hess, S., Mancini, M., Leblanc, F., Chaufray, J. Y., Brain, D., Leclercq, L., Esteban-Hernández, R., Chanteur, G., Weill, P., González-Galindo, F., Forget, F., Yagi, M., & Mazelle, C. (2016). Mars-solar wind interaction: LatHyS, an improved parallel 3-D multispecies hybrid

model. *Journal of Geophysical Research: Space Physics*, **121**, 6378–6399. https://doi.org/10.1002/2015JA022324

Morschhauser, A., Lesur, V., and Grott, M. (2014), A spherical harmonic model of the lithospheric magnetic field of Mars, *J. Geophys. Res. Planets*, 119, 1162– 1188, doi:10.1002/2013JE004555.

Najib, D., Nagy, A. F., Tóth, G., & Ma, Y.(2011). Three-dimensional, multifluid, high spatial resolution MHD model studies of the solar wind interaction with Mars. *Journal of Geophysical Research*, **116**, A05204. https://doi.org/10.1029/2010JA016272

Nagy, A., et al. (2004), The plasma environment of Mars, Space Sci. Rev., 111, 33–114

Nilsson, H., N. Edberg, G. Stenberg, and S. Barabash (2011), Heavy ion escape from Mars, influence from solar wind conditions and crustal magnetic fields, *Icarus*, doi:10.1016/j.icarus.2011.08.003.

Pilinski, M., Bougher, S., Greer, K., Thiemann, E., Andersson, L., Benna, M., & Elrod, M. (2018). First evidence of persistent nighttime temperature structures in the neutral thermosphere of Mars. *Geophysical Research Letters*, 45, 8819– 8825. https://doi.org/10.1029/2018GL078761

Ramstad, R., Y. Futaana, S. Barabash, H. Nilsson, S. M. del Campo B, R. Lundin, and K. Schwingenschuh (2013), Phobos 2/ASPERA data revisited: Planetary ion escape rate from Mars near the 1989 solar maximum, *Geophys. Res. Lett.*, **40**, 477–481, doi:10.1002/grl.50149.

Sakai, S., et al. (2016), Electron energetics in the Martian dayside ionosphere: Model comparisons with MAVEN data, *J. Geophys. Res. Space Physics*, 121, 7049– 7066, doi:10.1002/2016JA022782.

Schunk, R. W., and A. F. Nagy (2009), *Ionospheres: Physics, Plasma Physics, and Chemistry*, 2nd ed., Cambridge Univ. Press, Cambridge, U. K.

Strangeway, R. J., R. E. Ergun, Y.-J. Su, C. W. Carlson, and R. C. Elphic (2005), Factors controlling ionospheric outflows as observed at intermediate altitudes, *J. Geophys. Res.*, 110, A03221, doi:10.1029/2004JA010829.

Toth, G., et al. (2012), Adaptive numerical algorithms in space weather modeling, Journal of Computational Physics, Volume 231, Issue 3, 1 February 2012, Pages 870-903, ISSN 0021-9991, 10.1016/j.jcp.2011.02.006.

Trotignon, J. G., C. Mazelle, C. Bertucci, and M. H. Acuña (2006), Martian shock and magnetic pile-up boundary positions and shapes determined from the Phobos 2 and Mars Global Surveyor data sets, *Planet. Space Sci.*, **54**, 357–369, doi:10.1016/j.pss.2006.01.003.

Vignes, D., et al. (2000), The solar wind interaction with Mars: Locations and shapes of the bow shock and the magnetic pile-up boundary from the observations of the mag/er experiment onboard mars global surveyor, Geophys. Res. Lett., **27**(1), 49–52, doi:10.1029/1999GL010703.

Welling, D. T., André, M., Dandouras, I., Delcourt, D., Fazakerley, A., Fontaine, D., et al. (2015). The Earth: Plasma sources, losses, and transport processes. *Space Science Reviews*, **192**(1-4), 145–208.

Xu, S., Mitchell, D. L., Mcfadden, J. P., Collinson, G., Harada, Y., Lillis, R., et al. (2018). Field-aligned potentials at Mars from MAVEN observations. Geophysical Research Letters, 45, 10,119– 10,127. https://doi.org/10.1029/2018GL080136

Xu, S., Liemohn, M. W., & Mitchell, D. L.(2014). Solar wind electron precipitation into the dayside Martian upper atmosphere through the cusps of strong crustal fields. *Journal of Geophysical Research: Space Physics*, **119**, 10,100–10,115. https://doi.org/10.1002/2014JA020363

Yau, A. W., Abe, T., & Peterson, W. (2007). The polar wind: Recent observations. Journal of Atmospheric and Solar-Terrestrial Physics, 69 (16), 1936–1983. https://doi.org/10.1016/j.jastp.2007.08.010, recent Advances in the Polar Wind Theories and Observations.

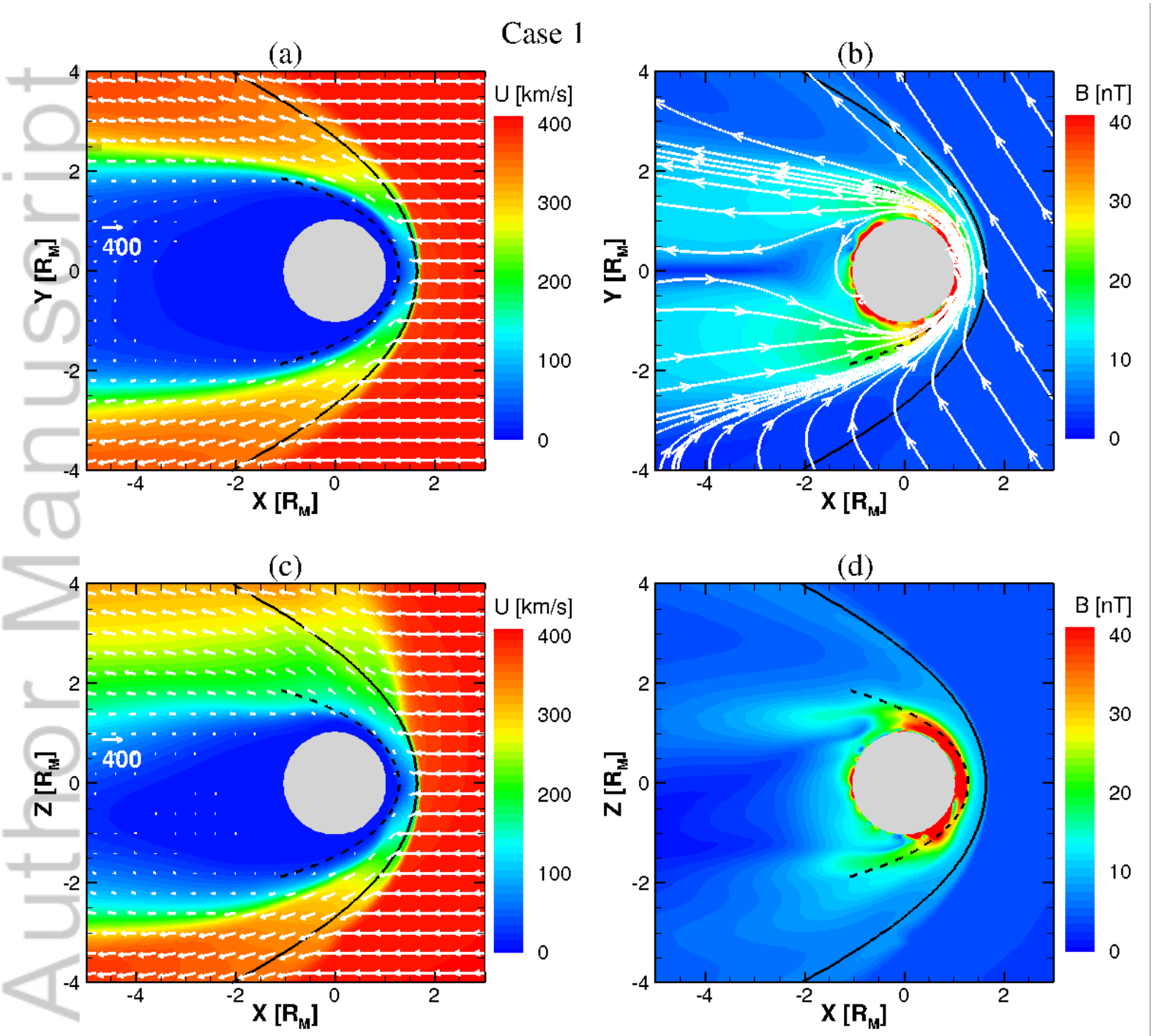

2019JA027091-f01-z-.tif

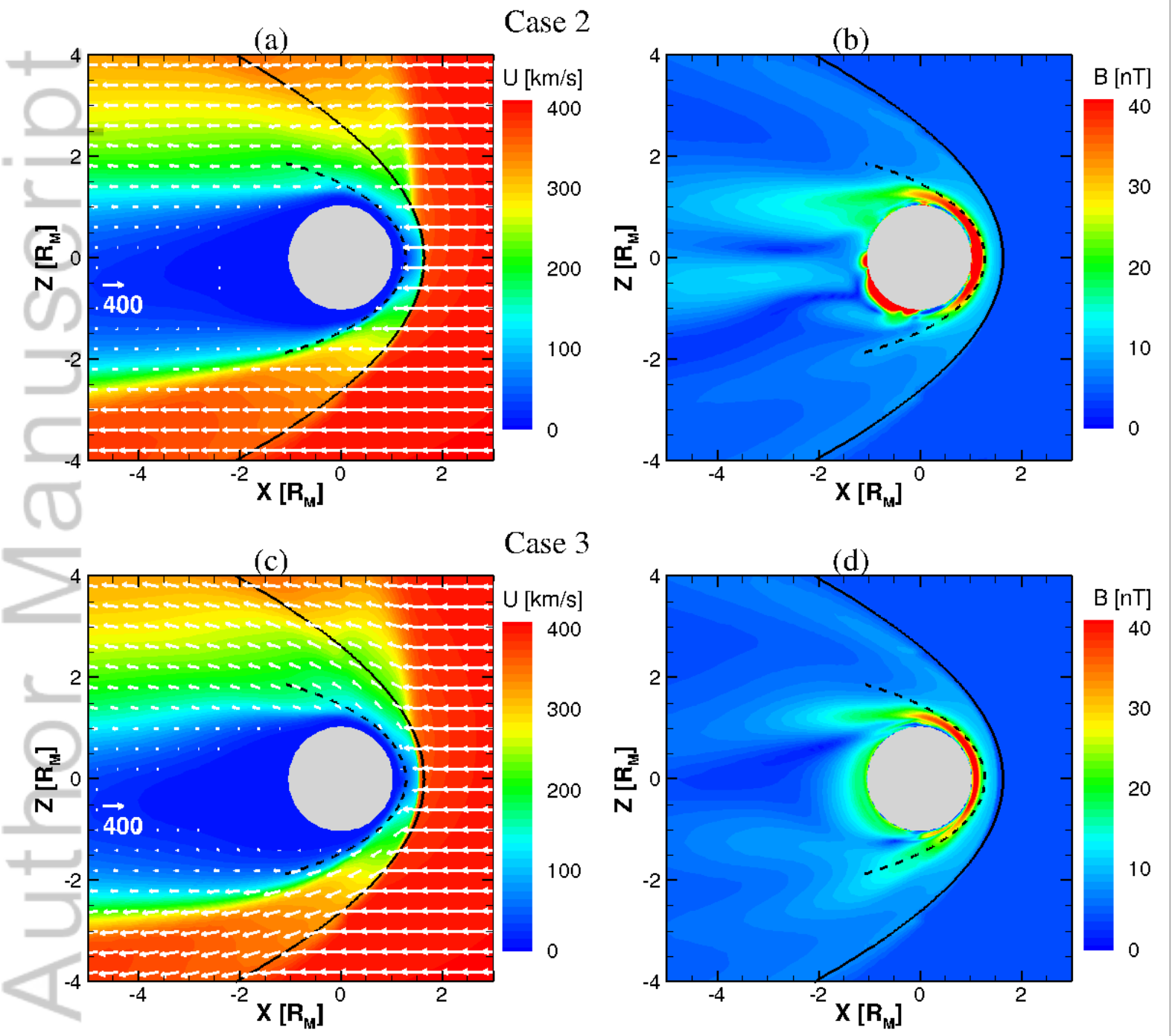

2019JA027091-f02-z-.tif

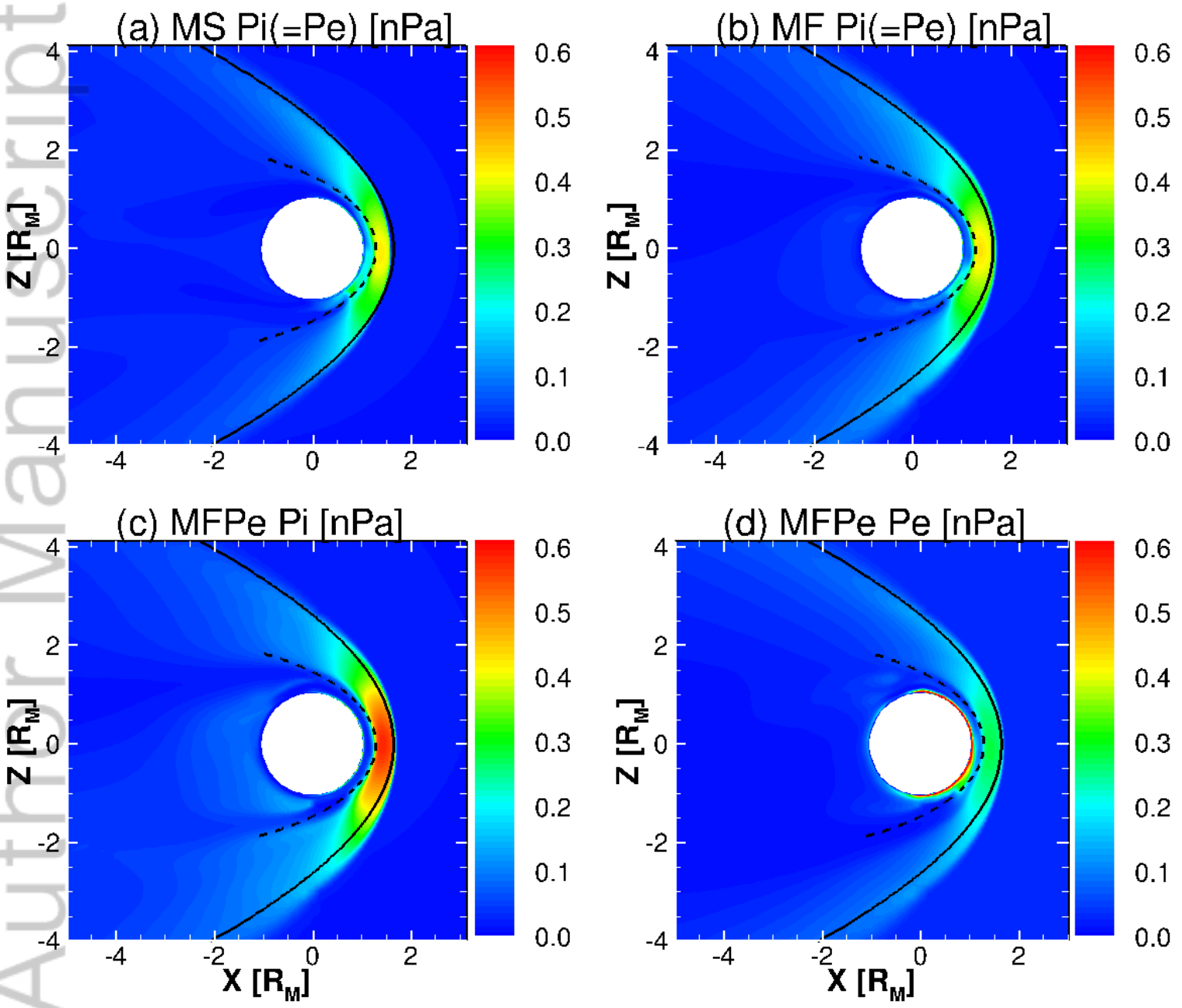

2019JA027091-f03-z-.tif

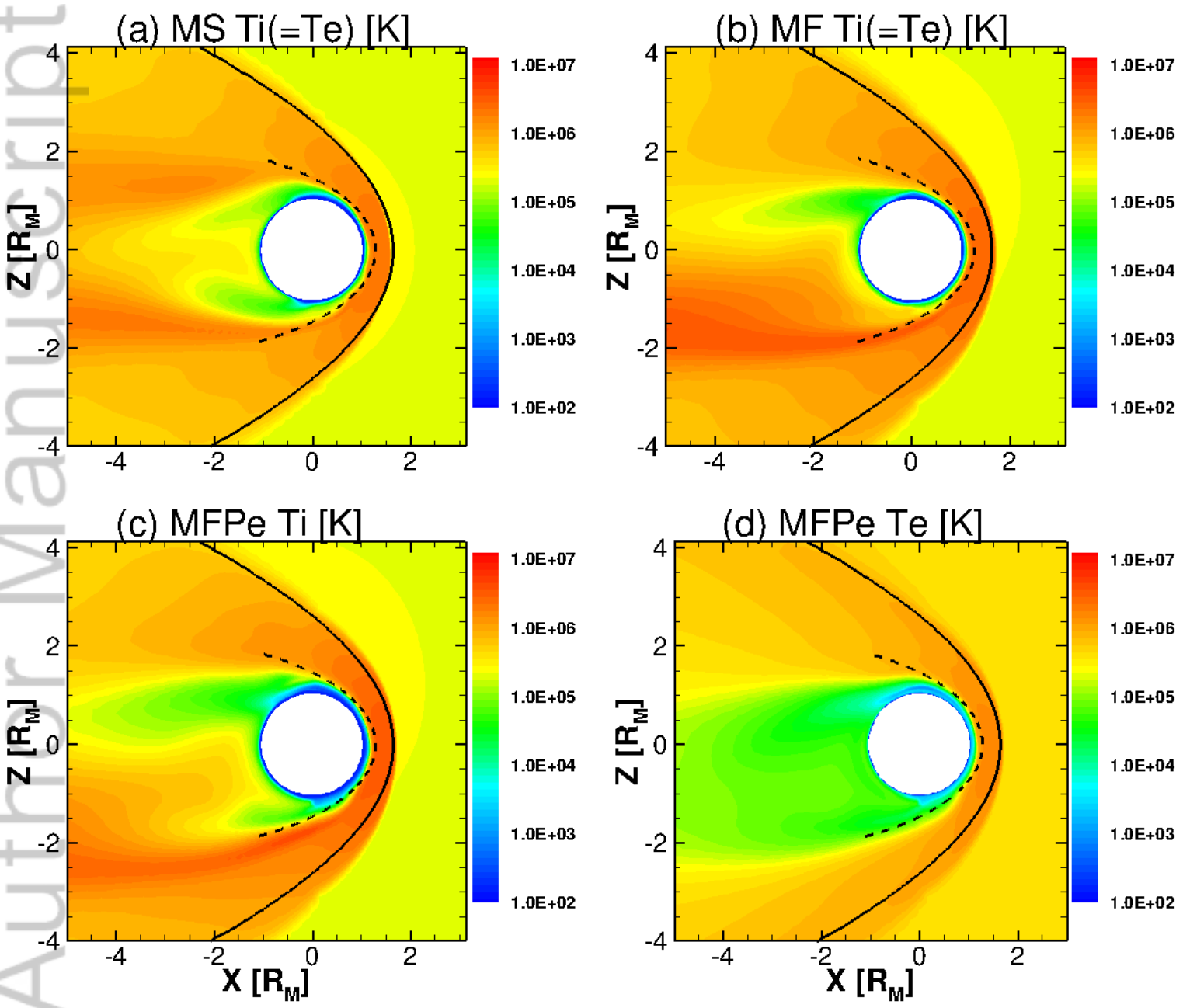

2019JA027091-f04-z-.tif

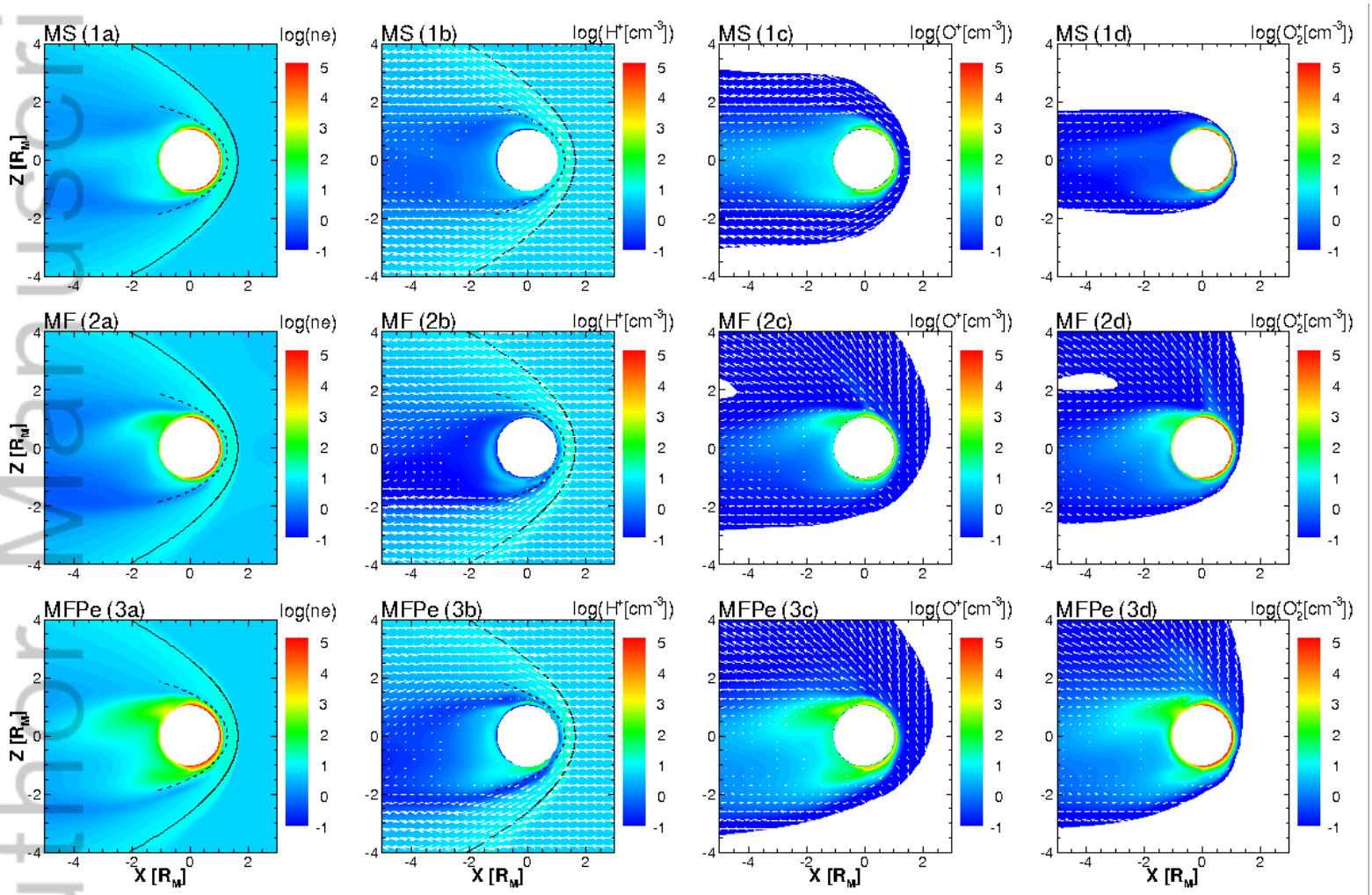

2019JA027091-f05-z-.tif

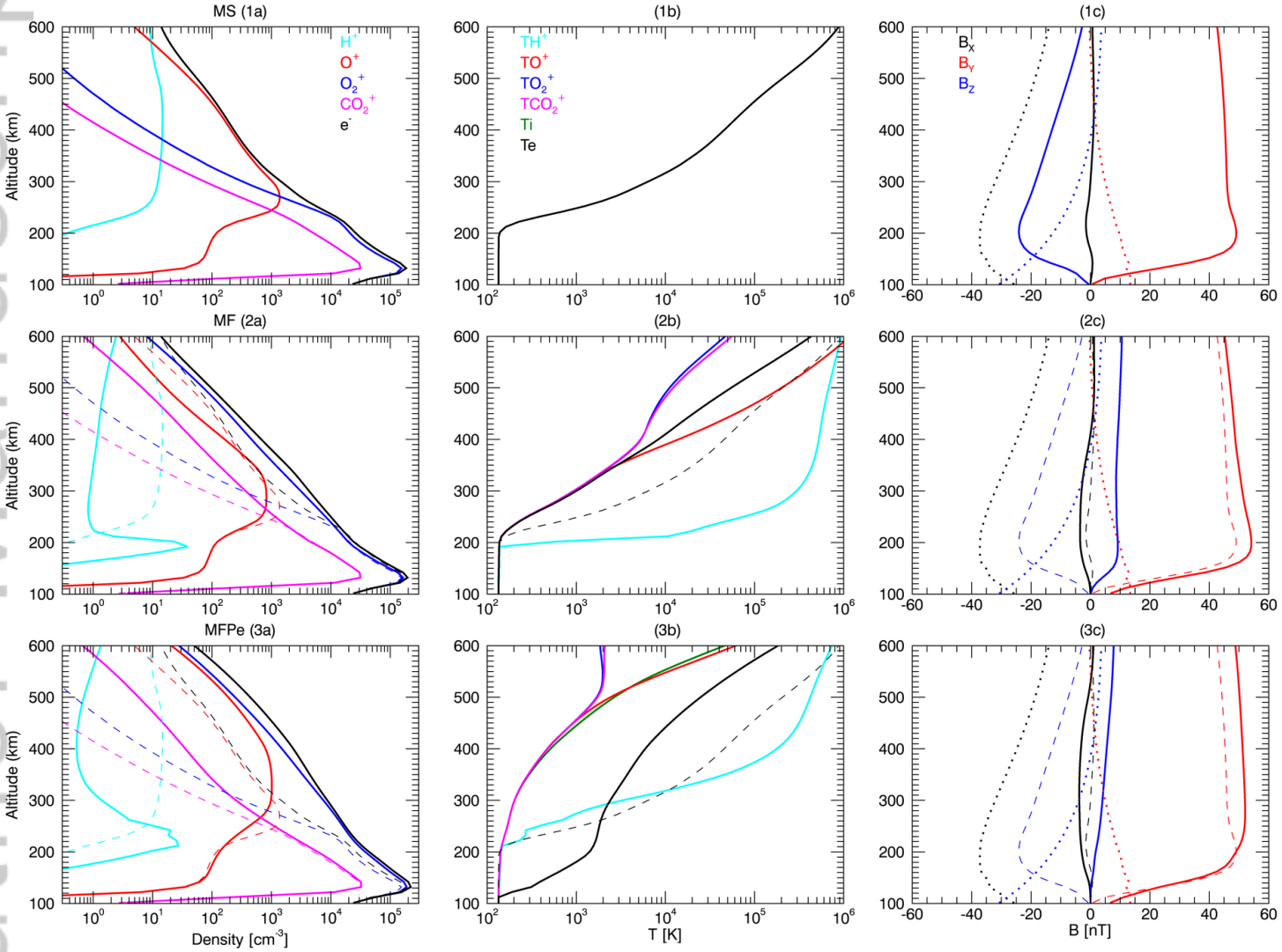

2019JA027091-f06-z-.png

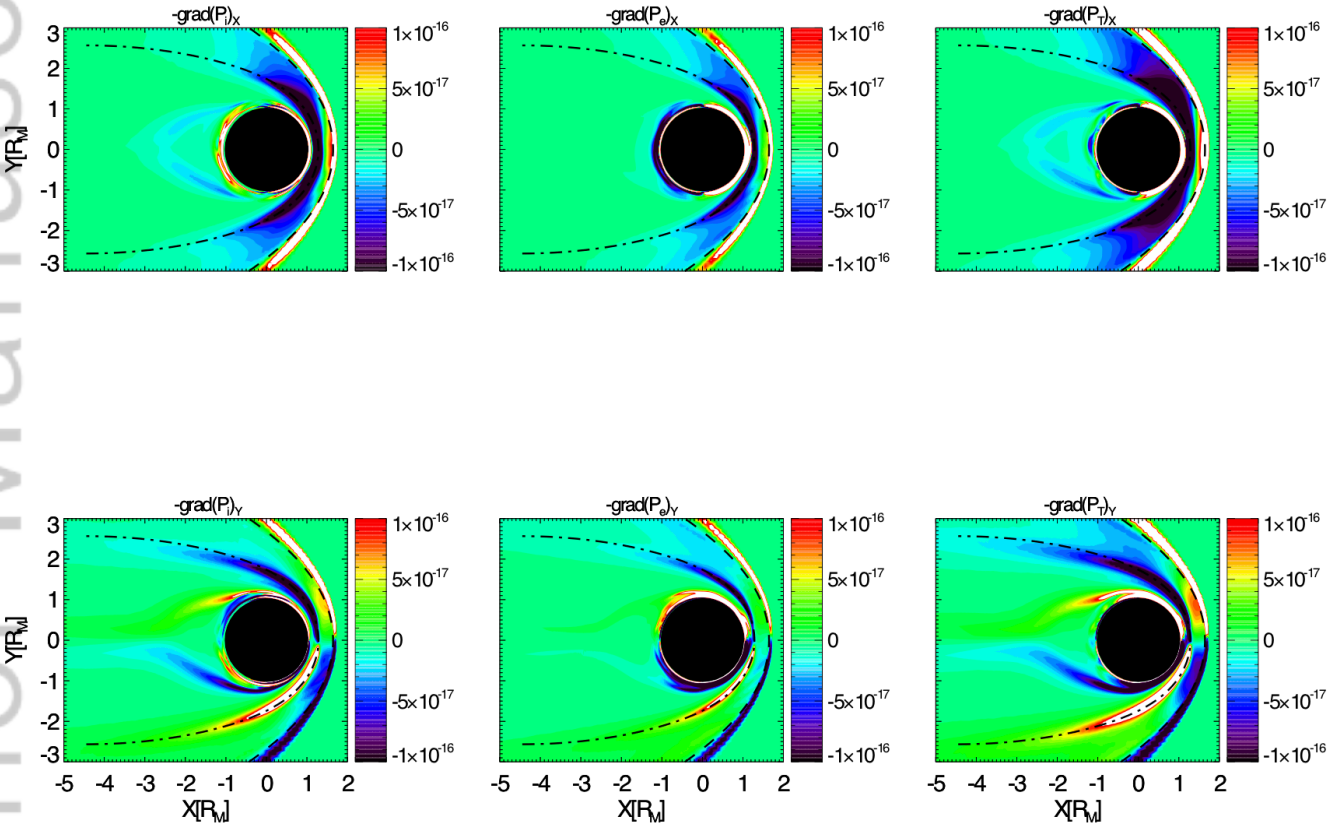

2019JA027091-f07-z-.tif

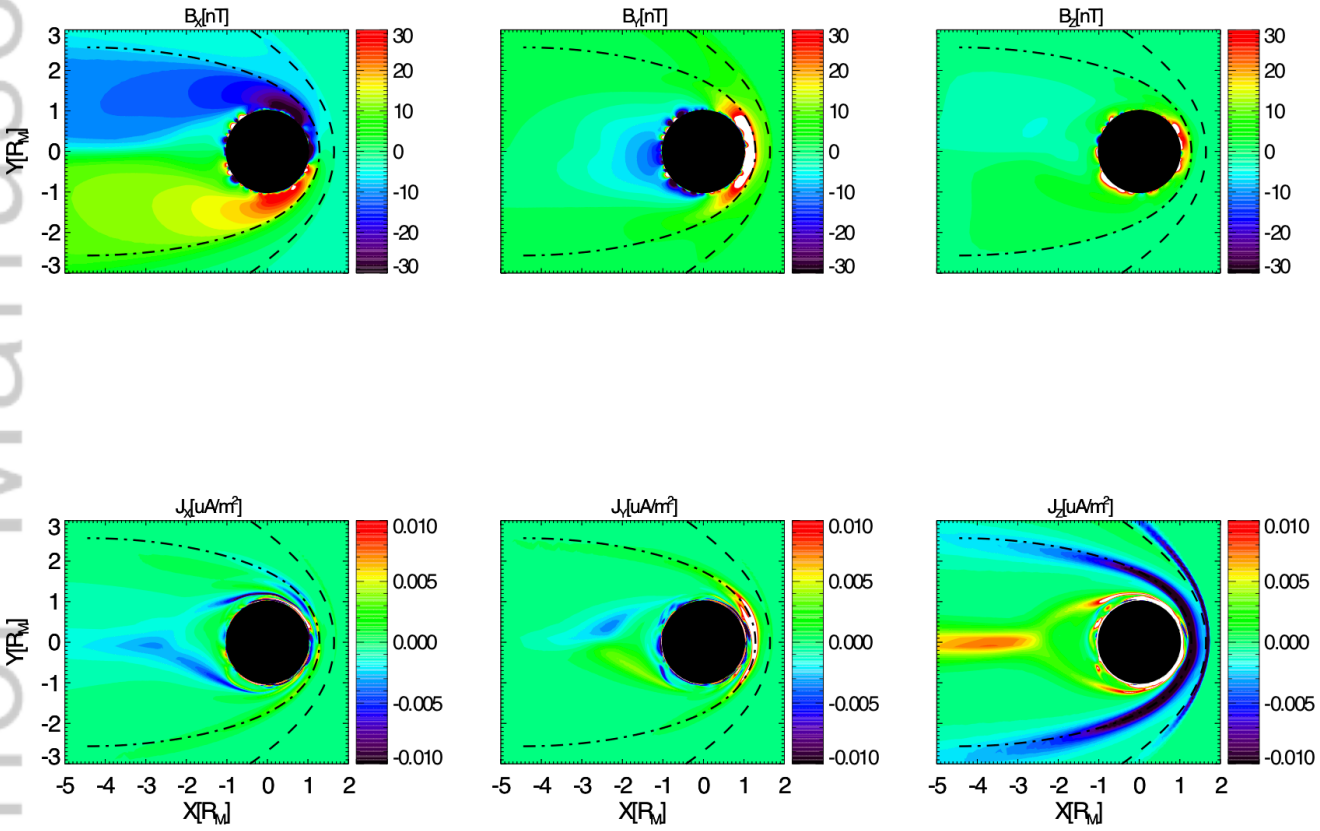

2019JA027091-f08-z-.tif

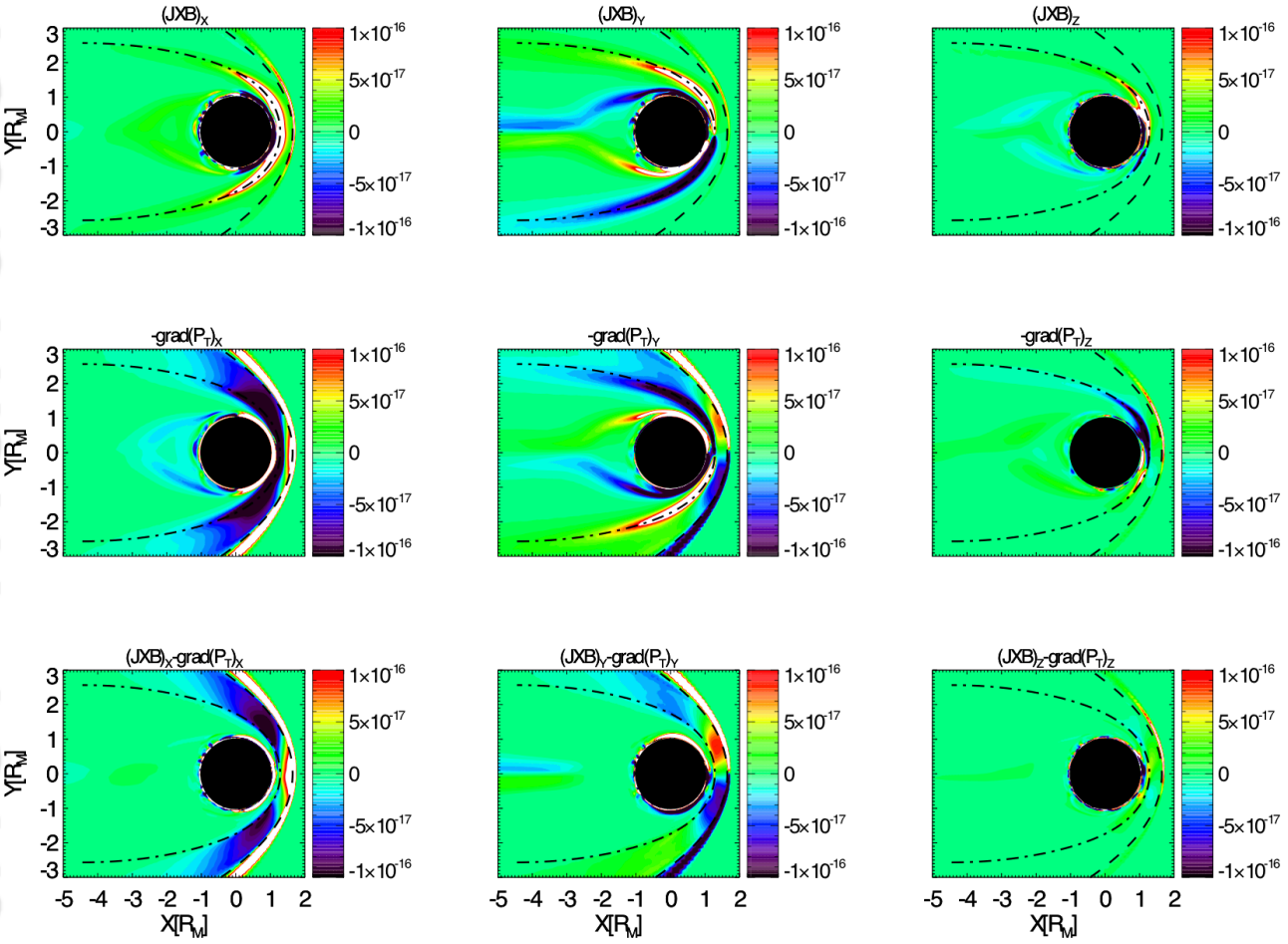

2019JA027091-f09-z-.tif

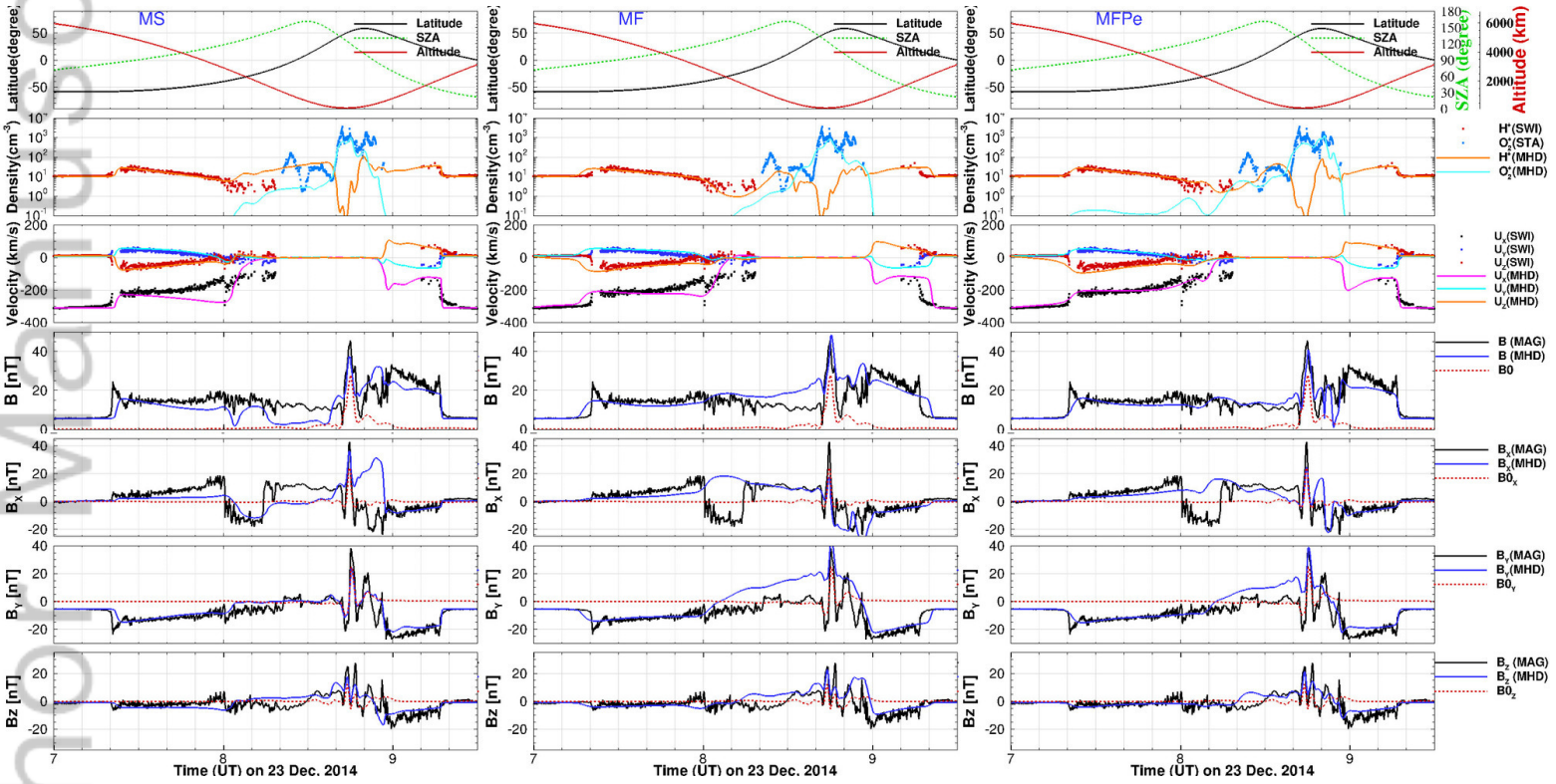

2019JA027091-f10-z-.jpg